

Comparison of cell- and vertex-centered finite-volume schemes for flow in fractured porous media

Dennis Gläser^a, Martin Schneider^a, Bernd Flemisch^a, Rainer Helmig^a

^a*Institute for Modelling Hydraulic and Environmental Systems, University of Stuttgart, Pfaffenwaldring 61, 70569 Stuttgart, Germany*

Abstract

Flow in fractured porous media is of high relevance in a variety of geotechnical applications, given the fact that they ubiquitously occur in nature and that they can have a substantial impact on the hydraulic properties of rock. As a response to this, an active field of research has developed over the past decades, focussing on the development of mathematical models and numerical methods to describe and simulate the flow processes in fractured rock. In this work, we present a comparison of different finite volume-based numerical schemes for the simulation of flow in fractured porous media by means of numerical experiments. Two novel vertex-centered approaches are presented and compared to well-established numerical schemes in terms of convergence behaviour and their performance on benchmark studies taken from the literature. The new schemes show to produce results that are in good agreement with those of established methods while being computationally less expensive on unstructured simplex grids.

Keywords: porous media, fractures, discrete fractures, coupling, finite volumes, box scheme

1. Introduction

Fractures are a common feature in many geological formations throughout the planet, and therefore, they are of particular importance in a wide range of geotechnical applications from groundwater management over energy production and storage to the disposal of waste (Berkowitz, 2002). Although fractures are typically characterized by rather small apertures, they can have significant lateral extents and form interconnected networks that have substantial influence on the overall hydraulic and mechanical behavior of rock (Jaeger et al., 2007). Besides naturally occurring fractures, they might also be introduced into a rock mass as a consequence of human activities, which is the case, for instance, in geothermal energy or unconventional shale gas production techniques. In the context of radioactive waste disposal, fractures can occur in the vicinity of emplacement tunnels as a consequence of their excavation, and thus, they have to be taken into account in safety assessment efforts (Lisjak et al., 2016).

As a response to the importance of fractures, a number of modelling approaches and simulation tools have been developed over the past decades. Typically, the approaches are classified into continuum fracture models and discrete fracture matrix (dfm) models. In the first class of models, the fracture geometry is not explicitly captured, but the overall medium is described in terms of effective properties in so-called single-continuum models (Pruess et al., 1990; Royer et al., 2002) or by describing the fracture network with one or more individual overlapping continua in dual- or multi-continuum models (Warren & Root, 1963; Kazemi et al., 1976; Pruess, 1992; Zimmerman

*Corresponding author

Email addresses: dennis.glaeser@iws.uni-stuttgart.de (Dennis Gläser), martin.schneider@iws.uni-stuttgart.de (Martin Schneider), bernd.flemisch@iws.uni-stuttgart.de (Bernd Flemisch), rainer.helmig@iws.uni-stuttgart.de (Rainer Helmig)

et al., 1993). In dfm models, the geometries of the most important fractures are resolved, while small scale fractures might still be accounted for by means of effective properties or additional continua. This allows for an explicit representation of fractures whose sizes are comparable to that of the domain and which are difficult to upscale, while maintaining the computational efficiency of continuum approaches where applicable. In such models, the fractures are incorporated either by describing them as heterogeneities in the rock, resolving the interior of the fractures with the computational mesh (Matthai et al., 2007), or as lower-dimensional interfaces embedded in the bulk medium. The latter approach has received significant attention in the past and a variety of models and numerical schemes have been developed, which can be further subdivided into conforming and non-conforming models. In the former, the computational grid used in the bulk medium is constrained such that the grid element faces are aligned with the fractures, while in the latter, bulk medium and fractures can be discretized independently. Examples for conforming approaches can be found, for instance, in Karimi-Fard et al. (2004); Martin et al. (2005); Sandve et al. (2012); Ahmed et al. (2015, 2017); Brenner et al. (2016); Boon et al. (2018); Nordbotten et al. (2019), while non-conforming models are the subject of Schwenck et al. (2015); Flemisch et al. (2016); Tene et al. (2017); Köppel et al. (2018); Schädle et al. (2019). While mesh generation is much simpler for non-conforming methods, they might struggle to capture relevant phenomena in the case of low-permeable fractures that act as barriers for flow.

In this work, we consider conforming approaches, and compare several cell- and vertex-centered numerical schemes in terms of accuracy and computational efficiency. Some of the schemes were presented in the references mentioned above, while two of the vertex-centered schemes, to the authors' knowledge, have not yet been introduced. Therefore, they receive special attention in this work. All schemes have been implemented into the same software framework, namely DuMu^x (Flemisch et al., 2011; Koch et al., 2020), and all computations have been carried out on the same machine, which allows for an easier comparison of the computational cost. We investigate the convergence behavior of the schemes against analytical and equi-dimensional reference solutions, and apply them to benchmark cases published in Flemisch et al. (2018); Berre et al. (2021), which enables us to compare the results to those of a large number of numerical schemes.

This paper is structured as follows. In section 2, we present the equi-dimensional mathematical model for flow in fractured porous media, where the fractures are treated as heterogeneities. Subsequently, the mixed-dimensional approximation of the model is presented in section 3. We briefly describe the considered numerical schemes in section 4, and provide a more detailed description of the novel vertex-centered schemes. Section 5 contains the numerical examples, and we conclude the paper in section 6 with a summary and outlook.

2. Equi-dimensional model

Let us consider a domain $\Omega \subset \mathbb{R}^3$ with boundary $\partial\Omega$. Furthermore, let Ω_b , Ω_f , Ω_{is} and Ω_j be disjoint partitions of Ω representing the bulk porous medium, the fractures, the intersections of fractures and the intersections of intersections, respectively. For the sake of readability, we will use the term junctions to refer to the intersections of intersections. The external subdomain boundaries are denoted by $\Gamma_b := \partial\Omega_b \cap \partial\Omega$, $\Gamma_f := \partial\Omega_f \cap \partial\Omega$ and $\Gamma_{is} := \partial\Omega_{is} \cap \partial\Omega$. For simplicity, we assume that junctions do not occur on the external boundary, i.e. it is $\Gamma_j := \partial\Omega_j \cap \partial\Omega = \emptyset$. The interfaces between subdomains are defined as $\gamma_{k,l} = \partial\Omega_k \cap \partial\Omega_l$, where $k \neq l$ and $k, l \in \{b, f, is, j\}$. We furthermore define the normal vectors on the interfaces $\gamma_{k,l}$ to be pointing outwards of the domains Ω_k . A two-dimensional illustration of this decomposition is depicted in fig. 1. Let us further decompose the external sub-domain boundaries $\Gamma_b = \Gamma_b^D \cup \Gamma_b^N$, $\Gamma_f = \Gamma_f^D \cup \Gamma_f^N$ and $\Gamma_{is} = \Gamma_{is}^D \cup \Gamma_{is}^N$ to indicate whether Dirichlet (superscript D) or Neumann (superscript N) boundary conditions are imposed. We require $|\Gamma_l^D| > 0$ for at least one subdomain $l \in \{b, f, is\}$.

The decomposition of the domain as described above might lead to the subdomains being composed of several disconnected sets. For instance, in the situation illustrated in fig. 1, the bulk

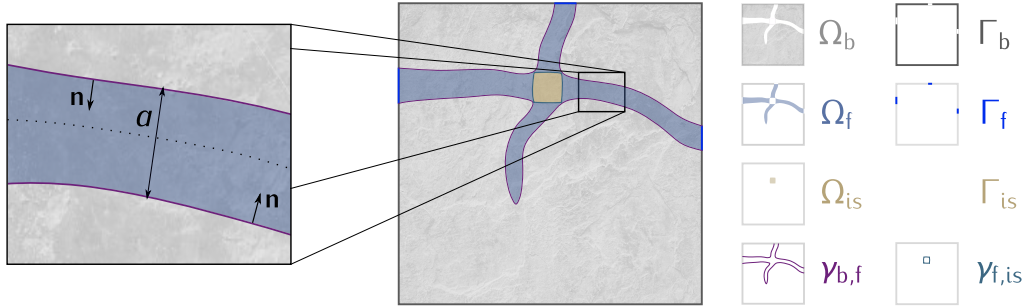


Figure 1: **Equi-dimensional domain decomposition.** The domain Ω is decomposed into the disjoint partitions Ω_f for the fractures, Ω_{is} for the fracture intersections and Ω_b for the surrounding bulk porous medium. The interfaces between the domains are denoted by $\gamma_{b,f}$ and $\gamma_{f,is}$ while the external boundaries of the sub-domains are denoted by Γ_b , Γ_f and Γ_{is} , respectively. Furthermore, the close-up on the left illustrates the fracture aperture a . In a two-dimensional setting, junctions of fracture intersections do not occur and are not visualized here. Please also note that the thickness of the fractures is exaggerated in this figure for illustrative purposes.

domain is partitioned into three and the fracture domain into four subsets. We make this apparent in the notation by equipping the subdomains with the superscript i indicating the index within the partition of a subdomain, i.e. it is $\Omega_k = \bigcup_{i \in I_k} \Omega_k^i$, where $I_k = \{0, 1, \dots, n_k\}$ and $k \in \{b, f, is, j\}$. Consequently, let us introduce the interfaces between subsets $\gamma_{k,l}^{i,j} = \partial\Omega_k^i \cap \partial\Omega_l^j$, $k \neq l$, $i \in I_k$ and $j \in I_l$, where we note that $\gamma_{k,l} = \bigcup_{j \in I_l} \gamma_{k,l}^{i,j}$. In this setting, we state the equi-dimensional formulation for single-phase flow:

$$\mathbf{q}_k^i + \mathbf{K}_k^i \nabla h_k^i = 0, \quad (1a)$$

$$\nabla \cdot \mathbf{q}_k^i = q_k^i, \quad \text{in } \Omega_k^i, \quad (1b)$$

$$h_k^i = h_l^j, \quad (1c)$$

$$\mathbf{q}_k^i \cdot \mathbf{n} = \mathbf{q}_l^j \cdot \mathbf{n}, \quad \text{on } \gamma_{k,l}^{i,j}, \quad (1d)$$

$$h_k^i = h_k^D, \quad \text{on } \Gamma_k^D \cap \partial\Omega_k^i, \quad (1e)$$

$$\mathbf{q}_k^i \cdot \mathbf{n} = f_k^i, \quad \text{on } \Gamma_k^N \cap \partial\Omega_k^i, \quad (1f)$$

where $i \in I_k$, $j \in I_l$, $k, l \in \{b, f, is, j\}$ and $l \neq k$. Equation (1a) states that Darcy's Law is used in all subdomains to relate the flux \mathbf{q} (given in $\text{m}^3/(\text{s}\cdot\text{m}^2)$) to gradients in the hydraulic head h (given in m), with \mathbf{K} being the hydraulic conductivity given in m/s. Equation (1b) states the conservation of mass in each subdomain, with q denoting sources or sinks in 1/s. Equations (1c) and (1d) state the interface conditions between different subdomains, which comprise of the continuity of the hydraulic head and fluxes. Finally, eqs. (1e) and (1f) state the Dirichlet and Neumann boundary conditions on the external boundaries.

In the subsequent section, we present the mixed-dimensional formulation that approximates the model given in (1). The notation that we will use is strongly influenced by the presentations given in Flemisch et al. (2018); Nordbotten et al. (2019).

3. Mixed-dimensional model

We now want to approximate the subdomains of the equi-dimensional setting for the fractures, fracture intersections and junctions of intersections, i.e. Ω_f , Ω_{is} and Ω_j , by lower-dimensional geometries. More precisely, the fractures are approximated by 2-dimensional entities that are constructed such that they follow the planes that describe the center of the fractures. Correspondingly, the intersections of fractures are approximated by 1-dimensional segments that describe center lines of the intersection regions between fractures and the junctions are approximated by 0-dimensional

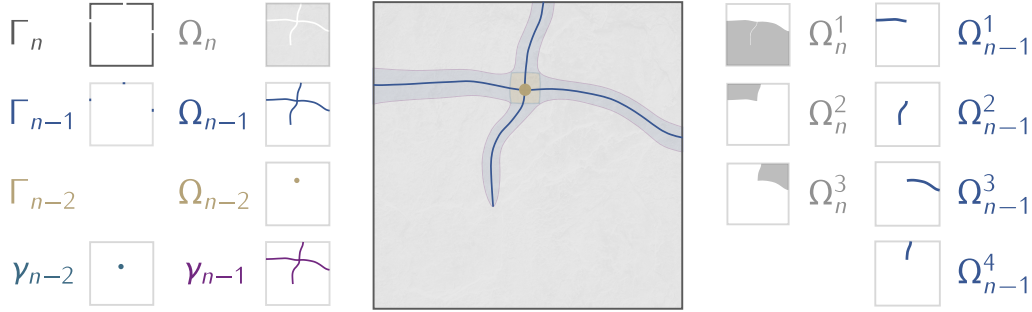


Figure 2: **Mixed-dimensional domain decomposition.** The domain Ω , illustrated in fig. 1 and depicted transparent here, is approximated by a mixed-dimensional decomposition consisting of an n -dimensional subdomain Ω_n for the bulk porous medium and the lower-dimensional subdomains Ω_{n-1} for the fractures and Ω_{n-2} for the intersections of fractures. Each subdomain is potentially split into disconnected subsets Ω_d^i , which are illustrated on the right. The interfaces between d - and $(d-1)$ -dimensional subdomains are denoted by γ_{d-1} , while the external boundaries of the sub-domains are denoted by Γ_d . Note that in two-dimensional settings, junctions of intersections do not occur which is why they are not visualized here.

points located at their center. In this mixed-dimensional setting, we will from now on refer to the sub-domains with the subscript d indicating the dimension, i.e. the original domain Ω is split into a 3-dimensional bulk domain Ω_3 , as well as the lower-dimensional domains Ω_2 , Ω_1 and Ω_0 for the fractures, their intersections and junctions of intersections, respectively. The external boundaries of the subdomains are denoted by $\Gamma_d = \partial\Omega_d \cap \partial\Omega$, where we note that $\partial\Omega_0 = \Gamma_0 = \emptyset$. Please note that in this mixed-dimensional setting, there can also occur immersed boundaries (fracture tips) $\hat{\Gamma}_2 = \partial\Omega_2 \setminus \Gamma_2$ and $\hat{\Gamma}_1 = \partial\Omega_1 \setminus \Gamma_1$, and we extend the notation to the highest-dimensional domain by defining $\hat{\Gamma}_3 = \emptyset$. A two-dimensional illustration of this decomposition of Ω is given in fig. 2.

A first simplification with respect to the equi-dimensional setting is that we only consider interfaces between subdomains of codimension one, which we denote by $\gamma_d = \partial\Omega_{d+1} \cap \partial\Omega_d$, $0 \leq d < 3$, i.e. γ_2 , γ_1 and γ_0 denote the interface between the bulk domain and the fractures, the interface between the fractures and their intersections and the interface between intersections and junctions. The normal vectors on these interfaces are defined such that they point outwards of the higher-dimensional domains.

As for the equi-dimensional case, the subdomains Ω_d might comprise of several disconnected subsets, that is, Ω_d^i , $i \in I_d$, is a subset of Ω_d , and we denote by $\gamma_d^{i,j} = \partial\Omega_{d+1}^i \cap \partial\Omega_{d+1}^j$, $i \in I_{d+1}$, $j \in I_d$, an interface between two such subsets of codimension one. Let us further introduce for each Ω_d^i , $0 \leq d < 3$, the set of indices of the neighboring higher-dimensional subsets Ω_{d+1}^j :

$$\mathcal{N}_d^{i,\uparrow} = \{j \in I_{d+1} : \gamma_d^{j,i} \neq \emptyset\}. \quad (2)$$

Cross section-averaged quantities. At each point $\mathbf{x} \in \Omega_d$, $d < 3$, let $\epsilon_d = \epsilon_d(\mathbf{x})$ denote the cross section that describes the geometry of the equi-dimensional counterpart around that position. That is, ϵ_2 is a segment orthogonal to Ω_2 , whose measure is the fracture aperture a , i.e. $|\epsilon_2| = a$. Correspondingly, $|\epsilon_1|$ is the cross-sectional area of an intersection region of two or more fractures. Thus, we note that $|\epsilon_d|$ is given in m^{3-d} . Let us now define the cross section-averaged hydraulic head as

$$h_d^i = \frac{1}{|\epsilon_d^i|} \int_{\epsilon_d^i} h_k^i dx, \quad (3)$$

where h_k^i refers to the hydraulic head in the equi-dimensional setting, and we consider the tuples $(d, k) \in \mathcal{T} := \{(2, f), (1, is)\}$. Correspondingly, we denote by q_d^i the cross section average of the sources q_k^i appearing in eq. (1). It will become clear in the following paragraphs why the tuple $(0, j)$ is not considered in \mathcal{T} .

Cross section-integrated balance equations. Integration of the mass balance equation eq. (1b) over the cross sections ϵ_d , $1 \leq d < 3$, yields the PDEs describing the flow along the lower-dimensional domains Ω_d , for which a detailed derivation can be found in Martin et al. (2005). This leads to the lower-dimensional mass balances

$$\nabla_d \cdot (|\epsilon_d^i| \mathbf{q}_d^i) = |\epsilon_d^i| q_d^i + \llbracket \mathbf{q}_{d+1} \cdot \mathbf{n} \rrbracket_d^i, \quad (4)$$

with \mathbf{q}_d^i being the cross section-averaged flux, and $\nabla_d \cdot (*)$ denoting the divergence operator in tangential direction of Ω_d . The last term in eq. (4) describes the mass transfer with the surrounding higher-dimensional domain and appears as an additional source/sink term. It sums up all fluxes leaving or entering the neighboring $(d+1)$ -dimensional subdomain, i.e. we have:

$$\llbracket \mathbf{q}_{d+1} \cdot \mathbf{n} \rrbracket_d^i = \sum_{j \in \mathcal{N}_d^{i,\uparrow}} \sum_{l=1}^{m_d^{i,j}} \left(\mathbf{q}_{d+1}^j \cdot \mathbf{n} \right)_l, \quad (5)$$

where we note that $m_d^{i,j} \in \{1, 2\}$. That is because for a point on the lower-dimensional subdomain Ω_d , there might be two sides of it that are associated with the same higher-dimensional subset Ω_{d+1}^j . Such situations occur, for instance, around immersed fracture tips, as illustrated by subdomain Ω_{n-1}^2 in fig. 1, which is fully immersed in Ω_n^1 .

Under the assumption that \mathbf{K}_k is constant over the cross section ϵ_d , $(d, k) \in \mathcal{T}$, the cross section-averaged flux \mathbf{q}_d^i is given by

$$\mathbf{q}_d^i = -\mathbf{K}_d^i \nabla_d h_d^i, \quad (6)$$

where $\nabla_d (*)$ is the gradient operator in tangential direction of Ω_d , and \mathbf{K}_d^i is the tangential part of \mathbf{K}_k^i , that is, $\mathbf{K}_d^i = \mathbf{K}_k^i - \mathbf{N}_d \mathbf{K}_k^i$, with \mathbf{N}_d being the projection into the space normal to Ω_d . For the fracture domain it is $\mathbf{N}_2 = \mathbf{n}_2 \otimes \mathbf{n}_2$, where \mathbf{n}_2 is a vector normal to Ω_2 and \otimes is the dyadic product. For intersections, the normal space is defined by two normal vectors to Ω_1 that are themselves orthogonal to each other: $\mathbf{N}_1 = \mathbf{n}_{1,1} \otimes \mathbf{n}_{1,2}$. Correspondingly, let us denote the normal part by $\mathbf{K}_d^{i,\perp} = \mathbf{n} \otimes \mathbf{n} \mathbf{K}_k^i$. Please note that we assume the normal part $\mathbf{K}_d^{i,\perp}$ to be isotropic within the normal space. This is a necessary requirement for the mixed-dimensional coupling condition (11a) presented later.

Junctions of fracture intersections. In the model presented in this work, we assume continuity of the hydraulic head and fluxes across junctions of intersections:

$$h_1^i = h_1^j, \quad \text{on } \Omega_0^k, \quad k \in I_0, \quad i, j \in \mathcal{N}_0^{k,\uparrow}, \quad (7a)$$

$$0 = \sum_{i \in \mathcal{N}_0^{k,\uparrow}} \mathbf{q}_1^i \cdot \mathbf{n}, \quad \text{on } \Omega_0^k, \quad k \in I_0. \quad (7b)$$

Thus, we assume that the junctions are significantly more permeable than the adjacent fracture intersection branches. This assumption is mainly motivated by limitations of our current implementation, and other authors have used different conditions that capture possible jumps in the hydraulic head across junctions of intersections (Nordbotten et al., 2019; Keilegavlen et al., 2020).

Mixed-dimensional formulation. Until now, we have considered a three-dimensional domain, taking into account flow in the bulk medium, the fractures and fracture intersections, while assuming continuity of the hydraulic head and the flux across junctions of fracture intersections. In order to generalize the model, let $n \in \{2, 3\}$ denote the dimension of the bulk domain, and δ , $1 \leq \delta \leq n-1$, the dimension of the lowest-dimensional subdomain along which flow is taken into account. Moreover, we use eq. (4) to also describe flow in the bulk domain by using the following extensions to

the notation: $\nabla_n \cdot (*) := \nabla \cdot (*)$, $\nabla_n (*) := \nabla (*)$, $h_n := h_b$, $\mathbf{q}_n := \mathbf{q}_b$, $\mathbf{K}_n := \mathbf{K}_b$, $|\epsilon_n| = 1$ and $\llbracket \mathbf{q}_{n+1} \cdot \mathbf{n} \rrbracket_n := 0$. The mixed-dimensional problem formulation then reads, for $\delta \leq d \leq n$:

$$\mathbf{q}_d^i + \mathbf{K}_d^i \nabla_d h_d^i = 0, \quad (8a)$$

$$\nabla_d \cdot (|\epsilon_d^i| \mathbf{q}_d^i) = |\epsilon_d^i| q_d^i + \llbracket \mathbf{q}_{d+1} \cdot \mathbf{n} \rrbracket_d^i, \quad \text{in } \Omega_d^i, \quad (8b)$$

together with the boundary conditions

$$h_d^i = h_d^D, \quad \text{on } \Gamma_d^D \cap \partial \Omega_d^i, \quad (9a)$$

$$\mathbf{q}_d^i \cdot \mathbf{n} = f_d^i, \quad \text{on } \Gamma_d^N \cap \partial \Omega_d^i, \quad (9b)$$

$$\mathbf{q}_d^i \cdot \mathbf{n} = 0, \quad \text{on } \hat{\Gamma}_d \cap \partial \Omega_d^i, \quad (9c)$$

the conditions (7) at junctions of the lowest-dimensional domain:

$$h_\delta^i = h_\delta^j, \quad \text{on } \Omega_{\delta-1}^k, \quad k \in I_{\delta-1}, \quad i, j \in \mathcal{N}_{\delta-1}^{k, \uparrow}, \quad (10a)$$

$$0 = \sum_{i \in \mathcal{N}_{\delta-1}^{k, \uparrow}} \mathbf{q}_\delta^i \cdot \mathbf{n}, \quad \text{on } \Omega_{\delta-1}^k, \quad k \in I_{\delta-1}, \quad (10b)$$

and the interface conditions between subdomains, with $\delta \leq \tilde{d} < n$:

$$-\mathbf{n}^T \mathbf{K}_{\tilde{d}}^{j, \perp} \mathbf{n} \frac{h_{\tilde{d}}^j - h_{\tilde{d}+1}^i}{L_{\tilde{d}}^{j, \perp}} = \mathbf{q}_{\tilde{d}+1}^i \cdot \mathbf{n}, \quad \text{on } \gamma_{\tilde{d}}^{i, j} \in \mathcal{B}_{\tilde{d}}, \quad (11a)$$

$$h_{\tilde{d}}^j = h_{\tilde{d}+1}^i, \quad \text{on } \gamma_{\tilde{d}}^{i, j} \in \mathcal{H}_{\tilde{d}}. \quad (11b)$$

As can be seen in the above conditions, we distinguish two types of interfaces. In the set $\mathcal{H}_{\tilde{d}}$ we collect the interfaces for which the permeability in the lower-dimensional neighboring domain is much larger than in the higher-dimensional neighbor. In this case, the jump in hydraulic head across the lower-dimensional domain may be neglected, which is expressed by condition (11b). In particular, we want to use this condition on interfaces to open fractures or intersections, which are often modeled by using an aperture-dependent tangential permeability (Matthai et al., 2007; Ucar et al., 2018), but for which a normal permeability $\mathbf{K}_{\tilde{d}}^{j, \perp}$, $j \in I_{\tilde{d}}$, cannot be defined. The remaining interfaces are collected in the set $\mathcal{B}_{\tilde{d}}$, on which the continuity of the flux and the hydraulic head is enforced via condition (11a), where the normal flux inside the fracture or fracture intersections is expressed by means of the finite difference given on the left hand side. Therein, $L_{\tilde{d}}^{j, \perp}$ is a characteristic length scale associated with the distance of $\Omega_{\tilde{d}}$ to the corresponding interface in the equi-dimensional setting. For the fractures, this is half of the aperture, i.e. $L_{n-1}^{j, \perp} = a^j/2 = |\epsilon_{n-1}^j|/2$, while for fracture intersections (when $n = 3$), it might be different for each neighboring fracture branch. In this work, we use $L_1^{j, \perp} = \sqrt{|\epsilon_1|}/2$, but more complex approaches can be used if information on the intersection geometry is available (see e.g. Walton et al. (2017)). Note that condition (11a) corresponds to the one given in Martin et al. (2005) for $\xi = 1.0$, where ξ is a parameter of the model presented therein.

4. Discretization schemes

In this work, we compare several finite-volume based approaches for the discretization of the model problem stated in (8)-(11) on the basis of a set of test cases. Several schemes are taken into account, some of which have been presented in the literature, and some of which contain, to the authors' knowledge, novel features in the way they are presented in this work. In the following, we want to provide a short overview over the considered schemes, and subsequently, we will provide more details on the vertex-centered approaches introduced in this work. All schemes are implemented into the open-source simulation framework DuMu^x (Flemisch et al., 2011; Koch et al., 2020), and the source code to the numerical examples presented in this work can be found at git.iws.uni-stuttgart.de/dumux-pub/glaeser2020b. Note that a monolithic solution strategy is chosen, that is, all discrete equations are assembled into a single, block-structured, system matrix.

TPFA-DFM. This scheme is based on a cell-centered finite-volume scheme using the two-point flux approximation (TPFA), and was first introduced in Karimi-Fard et al. (2004). Further details can be found in Sandve et al. (2012).

MPFA-DFM. Also a cell-centered scheme, it differs from the TPFA-DFM scheme in the way the fluxes between the grid cells are computed. In particular, it uses the multi-point flux approximation (MPFA) technique presented in Aavatsmark (2002) for unfractured media, and extensions to fractured porous media as presented in Sandve et al. (2012); Ahmed et al. (2015). Moreover, it was used in the context of isothermal and non-isothermal two-phase flow in fractured porous media in Gläser et al. (2017); Gläser et al. (2019).

BOX-DFM. Based on the vertex-centered BOX scheme (see e.g. Hackbusch (1989); Helmig (1997)), the BOX-DFM scheme was introduced in Reichenberger et al. (2006) for two-phase flow in fractured porous media. The reduction to single-phase flow is straightforward, and we refer to Reichenberger et al. (2006); Tatomir (2012) for further details. It should be mentioned that this scheme does not exactly solve (8)-(11). Instead, continuity of the hydraulic head across the fractures (as expressed in eq. (11b)) is assumed. Therefore, no additional degrees of freedom with respect to the standard BOX scheme are introduced to describe the state inside the fracture. The effect of the fractures is incorporated by providing additional connectivity within the single mass balance equation that is solved for the bulk medium. This means, in particular, that eq. (8b) is not solved for the fracture domain, and that the condition eq. (11a) is not fulfilled at matrix-fracture interfaces. Moreover, the implementation as provided in DuMu^x does not allow for flow along fracture intersections to be considered.

EBOX-DFM. This scheme is an extension of the BOX scheme in the sense that additional degrees of freedom are introduced in and around the fractures, which allow for an incorporation of the conditions (11) at the matrix-fracture and fracture-intersection interfaces and the solution of the mass balance equations (8b) for the lower-dimensional domains, and which make it possible to capture the jump in fluxes and hydraulic head that can occur across low-permeable fractures. This scheme will be presented in more detail in section 4.2.

EBOX-MORTAR-DFM. We introduce the extended box scheme, the EBOX-DFM scheme, to overcome the drawbacks of the BOX-DFM scheme with respect to the incorporation of the interface conditions given in eq. (11). However, the conditions (11b) can only be incorporated weakly, as will be seen in section 4.2. To this end, the EBOX-MORTAR-DFM scheme was developed, in which an additional mortar variable representing the normal flux, is introduced on the interfaces between domains of different dimensionality. This enables a strong incorporation of the conditions (11). Details on this scheme will be provided in section 4.3.

In the following sections, we want to outline the basic concepts of the EBOX-DFM and the EBOX-MORTAR-DFM schemes. Section 4.1 presents the construction of the finite-volume discretizations of the subdomains, which is common to both schemes, and subsequently, the schemes are presented in sections 4.2 and 4.3.

4.1. Computational mesh

Let us introduce the primary discretizations \mathcal{M}_d , $\delta \leq d \leq n$, with elements $E \in \mathcal{M}_d$ such that $\tilde{\Omega}_{d,h} \equiv \bigcup_{E \in \mathcal{M}_d} \bar{E}$ are discrete approximations of Ω_d . Correspondingly, let \mathcal{M}_d^i be the subset of \mathcal{M}_d associated with the discrete subdomain $\Omega_{d,h}^i$. Moreover, let us denote with \mathcal{X}_d the set of faces of the primary discretization, and define the subsets \mathcal{X}_E such that for each element $E \in \mathcal{M}_d$ it is $\partial E = \bigcup_{\varsigma \in \mathcal{X}_E} \bar{\varsigma}$. We require the grids to be conforming such that the elements of the lower-dimensional domains coincide with faces of the next higher-dimensional domains, that is, we have $\forall E \in \mathcal{M}_d, d < n: \exists \varsigma \in \mathcal{X}_{d+1}$ such that $\varsigma \equiv E$. This is illustrated in fig. 3.

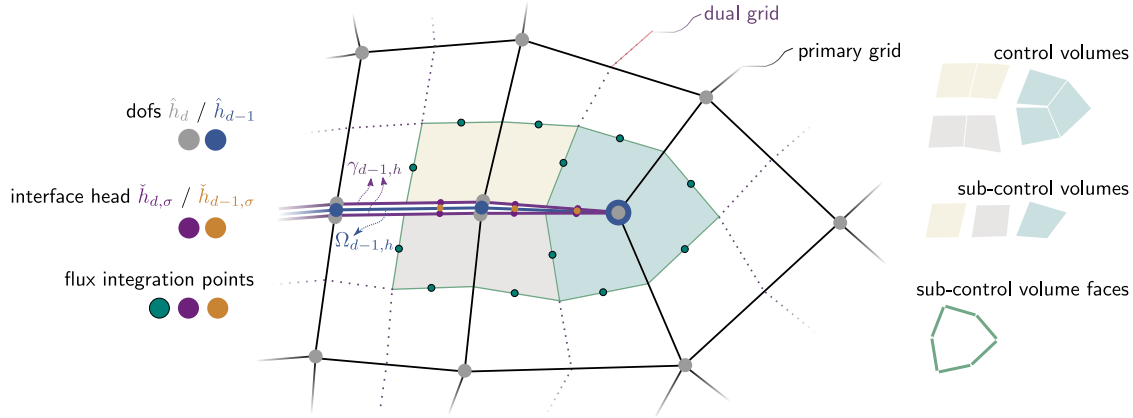


Figure 3: **Illustration of the ebox-dfm scheme.** Shown is an exemplary configuration around a fracture tip, depicting the distribution of the degrees of freedom, the subdivision of the control volumes into sub-control volumes, and the points at which fluxes are assembled. For illustration purposes, the fracture surfaces have been moved away from each other, separating the interface γ_{d-1} from the lower-dimensional domain Ω_{d-1} . They actually geometrically coincide in the discrete representation.

In addition to the primary grid, let us introduce the tessellations \mathcal{K}_d , composed of control volumes $K \in \mathcal{K}_d$ with measure $|K| > 0$ such that $\bigcup_{K \in \mathcal{K}_d} \bar{K} \equiv \bar{\Omega}_{d,h}$. As for the primary discretization, we denote by \mathcal{K}_d^i the subset associated with the discrete subdomain $\Omega_{h,d}^i$. While for cell-centered schemes it is $\mathcal{K}_d \equiv \mathcal{M}_d$, the BOX discretization is defined on a dual grid such that the elements and control volumes do not coincide. The dual grid is constructed by connecting the barycenters of the cells and edges (and in 3d also the faces) of the primary discretizations, as illustrated in fig. 3 for a two-dimensional setting, and the control volumes are defined by the emerging bounded regions around the grid vertices. In contrast to the standard BOX scheme, the control volumes in the BOX-DFM scheme might be split into two or more control volumes by intersecting fractures or intersections, which can be seen in the illustration given in fig. 3 for the two central control volumes. Each control volume has a unique degree of freedom associated with it, and correspondingly, additional degrees of freedom are introduced for each side of a fracture or intersection. Please note that this is not the case at fracture tips, at which a single degree of freedom per domain describes the hydraulic state.

Furthermore, we denote by \mathcal{S}_d the sets of faces of the tessellations \mathcal{K}_d , and define the subsets \mathcal{S}_K such that for a control volume $K \in \mathcal{K}_d$ it is $\partial K = \bigcup_{\sigma \in \mathcal{S}_K} \bar{\sigma}$. The corresponding unit normal vectors \mathbf{n}_K^σ are defined to be pointing outwards of K . Let us further define the subsets $\mathcal{S}_{d,c}$, $\mathcal{S}_{d,int}$ and $\mathcal{S}_{d,ext}$ of coupling faces that overlap with a $(d-1)$ -dimensional control volume $K \in \mathcal{K}_{d-1}$, internal faces and faces on the outer domain boundary, respectively. Moreover, we subdivide the set of coupling faces such that $\mathcal{S}_{d,c} = \mathcal{S}_{d,\mathcal{H}} \cup \mathcal{S}_{d,\mathcal{B}}$, where $\mathcal{S}_{d,\mathcal{H}}$ collects all coupling faces on which condition (11b) is enforced, while $\mathcal{S}_{d,\mathcal{B}}$ contains all faces on which eq. (11a) holds.

As a result of the construction of the dual grid, the control volumes overlap with several elements of the primary grid. We denote with κ a sub-control volume of the control volume K , where each κ can be associated to a primary grid element E such that $\kappa = K \cap E$. Let \mathcal{C}_d be the set of sub-control volumes of a discretization together with the subset \mathcal{C}_K such that $\bar{K} = \bigcup_{\kappa \in \mathcal{C}_K} \bar{\kappa}$.

4.2. Vertex-centered, discontinuous, finite-volume scheme (EBOX-DFM)

As in the standard BOX scheme, piecewise (per primary grid element) linear basis functions are used to approximate the hydraulic head and its gradients within the primary grid cells. For instance, the discrete approximation of the hydraulic head at a position $\mathbf{x} \in \Omega_{d,h}^i$ is expressed by:

$$\tilde{h}_d^i(\mathbf{x}) = \sum_{K \in \mathcal{K}_d^i} \hat{h}_K \varphi_K(\mathbf{x}), \quad (12)$$

where φ_K refers to the basis function that corresponds to the degree of freedom associated with the control volume K , and \hat{h}_K is the nodal value of the hydraulic head at that degree of freedom. The basis functions are defined as for continuous, linear finite elements, that is, $\varphi_K(\hat{\mathbf{x}}_K) = 1$, with $\hat{\mathbf{x}}_K$ being the position of the degree of freedom associated with control volume K (which is the position of the associated grid vertex), and $\varphi_K(\hat{\mathbf{x}}_L) = 0$, with $K, L \in \mathcal{K}_d$, $K \neq L$. Furthermore, the basis functions φ_K are only non-zero within primary grid elements that the control volume K overlaps with. Let us denote with \mathcal{K}_E the set of control volumes for which it is $K^\circ \cap E^\circ \neq \emptyset$, with $K \in \mathcal{K}_d$ and $E \in \mathcal{M}_d$. The discrete hydraulic head and its gradient, evaluated at a position $\mathbf{x} \in E$, $E \in \mathcal{M}_d^i$, can then be written as:

$$\tilde{h}_d^i(\mathbf{x}) = \sum_{K \in \mathcal{K}_E} \hat{h}_K \varphi_K(\mathbf{x}), \quad (13a)$$

$$\nabla_d \tilde{h}_d^i(\mathbf{x}) = \sum_{K \in \mathcal{K}_E} \hat{h}_K \nabla \varphi_K(\mathbf{x}). \quad (13b)$$

Discrete mass balance equation. Integration of eq. (8b) over a control volume $K \in \mathcal{K}_d^i$, applying the Gauss divergence theorem and splitting the resulting surface integral over the boundary of K into a sum over the faces $\sigma \in \mathcal{S}_K$, yields:

$$\sum_{\sigma \in \mathcal{S}_K} \int_{\sigma} |\epsilon_d^i| (\mathbf{q}_d^i \cdot \mathbf{n}_K^\sigma) \, d\Gamma = \int_K |\epsilon_d^i| q_d^i + \llbracket \mathbf{q}_{d+1} \cdot \mathbf{n} \rrbracket_d^i \, dV. \quad (14)$$

Moreover, the volume integrals in eq. (14) can be split into a sum over the sub-control volumes:

$$\sum_{\sigma \in \mathcal{S}_K} \int_{\sigma} |\epsilon_d^i| (\mathbf{q}_d^i \cdot \mathbf{n}_K^\sigma) \, d\Gamma = \sum_{\kappa \in \mathcal{C}_K} \int_{\kappa} |\epsilon_d^i| q_d^i + \llbracket \mathbf{q}_{d+1} \cdot \mathbf{n} \rrbracket_d^i \, dV. \quad (15)$$

Let us now use the notation $(*)_{\kappa}$ and $(*)_{\sigma}$ to denote quantities that are evaluated for a sub-control volume κ or a face σ , where we now omit the subscript related to the dimension, as the discrete entities carry the notion of the dimensionality of the grid on which they are defined. Following the same argumentation, we omit the superscript i referring to the subset $\Omega_{d,h}^i \subset \Omega_{d,h}$ on which a variable is defined. We will use this notation with any discrete entity, and it means that the quantity is taken as constant on that entity. With this, we can write the discrete balance equation for a control volume $K \in \mathcal{K}_d^i$ as follows:

$$\sum_{\sigma \in \mathcal{S}_K} F_K^\sigma = \sum_{\kappa \in \mathcal{C}_K} |\kappa| |\epsilon_\kappa| q_K + \llbracket F_{d+1} \rrbracket_{\kappa}, \quad (16)$$

where we have introduced the discrete flux

$$F_K^\sigma \approx - \int_{\sigma} |\epsilon_d^i| (\mathbf{n}_K^\sigma)^T \mathbf{K}_d^i \nabla_d h_d^i \, d\Gamma = \int_{\sigma} |\epsilon_d^i| (\mathbf{q}_d^i \cdot \mathbf{n}_K^\sigma) \, d\Gamma \quad (17)$$

as an approximation of the flux terms appearing in the sum on the left hand side of eq. (15), and where $\llbracket F_{d+1} \rrbracket_{\kappa}$ is the jump of the discrete flux in the adjacent higher-dimensional domain across the sub-control volume κ . That is, it is the sum over the discrete fluxes on all faces $\Xi \in \mathcal{S}_{K^\uparrow}$, embedded in the control volumes $K^\uparrow \in \mathcal{K}_{d+1}$, which overlap with κ such that $\kappa \equiv \Xi$.

Discrete flux expressions on internal faces. Using the expression for the discrete gradient given in eq. (13b), we define the discrete flux on internal faces $\sigma \in \mathcal{S}_{d,\text{int}}$, embedded in the control volume $K \in \mathcal{K}_d^i$, by:

$$F_K^\sigma = -|\sigma| |\epsilon_\kappa| (\mathbf{n}_K^\sigma)^T \mathbf{K}_\kappa \nabla_d \tilde{h}_d^i(\mathbf{x}_\sigma) \quad (18)$$

where \mathbf{x}_σ is the center point of the face σ . Here, κ refers to the sub-control volume adjacent to the face σ , that is, $\sigma \subset \bar{\kappa}$. Please note that we define the permeability and the cross-sectional measure to be constant per primary grid cell. Thus, on the sub-control volumes we inherit these properties, that is, we have $|\epsilon_\kappa| = |\epsilon_E|$ and $\mathbf{K}_\kappa = \mathbf{K}_E$ for $E \in \mathcal{M}_d^i$, $\kappa \in \mathcal{C}_K$, $K \in \mathcal{K}_d^i$, $\kappa \subset E$.

Discrete flux expressions on coupling faces. On coupling faces $\sigma \in \mathcal{S}_{d,\mathcal{B}}$, we want to enforce the condition (11a). To this end, we substitute the discrete flux by the finite difference given on the left hand side of eq. (11a):

$$F_K^\sigma = -|\sigma||\epsilon_\kappa| (\mathbf{n}_K^\sigma)^T \mathbf{K}_{\kappa^\downarrow}^\perp \mathbf{n}_K^\sigma \frac{\check{h}_{d-1,\sigma} - \check{h}_{d,\sigma}}{L_{\kappa^\downarrow}}. \quad (19)$$

Here, $\kappa^\downarrow \in \mathcal{C}_{d-1}$ refers to the lower-dimensional control volume that coincides with the face σ , i.e. $\sigma \equiv \kappa^\downarrow$, and $\check{h}_{d-1,\sigma} = \check{h}_{d-1}(\mathbf{x}_\sigma)$ and $\check{h}_{d,\sigma} = \check{h}_d(\mathbf{x}_\sigma)$ denote the discrete hydraulic heads evaluated at the center \mathbf{x}_σ of the face after eq. (13a).

The EBOX-DFM scheme does not allow for a strong incorporation of the conditions (11b) for the degrees of freedom that live on the interfaces to highly-permeable or open fractures or fracture intersections, while guaranteeing that the discrete mass balance equation (16) is fulfilled for the corresponding control volumes. Therefore, the condition can only be incorporated weakly, for instance, via a penalty term. However, this approach requires an adequate choice of the penalty parameter, where for large values, one typically runs into the problem that the conditioning of the linear system deteriorates and the solution of the problem becomes cumbersome, while for small values the desired condition of continuity of the hydraulic head might be significantly violated. In this work, we want to investigate a different approach. To this end, let us introduce the map

$$\mathcal{I} : \mathcal{K}_d \rightarrow \mathcal{K}_{d-1}, \quad \text{s.t. } \hat{\mathbf{x}}_K = \hat{\mathbf{x}}_{\mathcal{I}(K)}, \quad K \in \mathcal{K}_d, \quad (20)$$

which maps to each control volume $K \in \mathcal{K}_d$ that touches an interface to the adjacent $(d-1)$ -dimensional domain, the lower-dimensional control volume $L = \mathcal{I}(K)$ whose degree of freedom is located at the same geometric location. We then define the discrete flux on coupling faces $\sigma \in \mathcal{S}_{d,\mathcal{H}}$ on which the condition (11b) is to be used by

$$F_K^\sigma = -|\sigma||\epsilon_\kappa| (\mathbf{n}_K^\sigma)^T \mathbf{K}_\kappa \left[\sum_{\substack{K \in \mathcal{K}_E \\ \hat{\mathbf{x}}_K \notin \Omega_{d-1,h}}} \hat{h}_K \nabla \varphi_K(\mathbf{x}_\sigma) + \sum_{\substack{K \in \mathcal{K}_E \\ \hat{\mathbf{x}}_K \in \Omega_{d-1,h}}} \hat{h}_{\mathcal{I}(K)} \nabla \varphi_K(\mathbf{x}_\sigma) \right]. \quad (21)$$

Thus, for the assembly of the coupling fluxes, we substitute the nodal hydraulic heads for the degrees of freedom located on an interface with the nodal values at those locations on the lower-dimensional domain.

4.3. Vertex-centered, discontinuous, finite-volume scheme with flux mortars (EBOX-MORTAR-DFM)

In the presentation of the EBOX-DFM scheme, we have seen that it is not possible to strongly incorporate the coupling condition (11b) while maintaining local mass conservation. In order to overcome this issue, we now want to present an approach that introduces mortar variables at the interfaces γ_d between domains of different dimensionality, which represent the normal fluxes $\mathbf{q}_{d+1} \cdot \mathbf{n}$ across them. To this end, let Λ_d , $\delta \leq d < n$, denote the mortar variable defined on the interfaces between d - and $(d+1)$ -dimensional domains. We consider piecewise constant (per grid element) Λ_d , defined on the mesh \mathcal{M}_{Λ_d} , which overlaps with \mathcal{M}_d in a potentially nonconforming way. That is, the characteristic discretization lengths η_d and η_{Λ_d} of \mathcal{M}_d and \mathcal{M}_{Λ_d} might differ, and we will use the parameter $\psi = \eta_{\Lambda_d}/\eta_d$ to describe their ratio. An illustration of this is given in fig. 4.

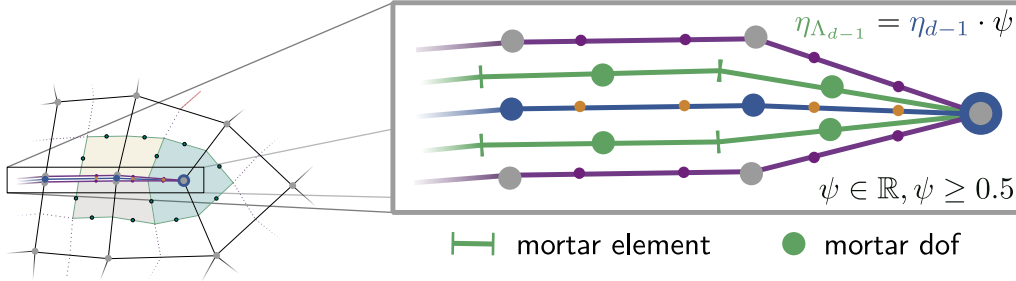


Figure 4: **Illustration of the ebox-mortar-dfm scheme.** In addition to the setting illustrated in fig. 3, the mortar variable Λ_{d-1} is introduced at the interfaces between the d - and $(d-1)$ -dimensional grids. The mortar variable Λ represents the normal flux across the interface, and is defined on the $(d-1)$ -dimensional grid $\mathcal{M}_{\Lambda_{d-1}}$, which is potentially nonconforming to \mathcal{M}_{d-1} , the grid used for flow. This is illustrated in the close-up given on the right hand side, where the discretization lengths $\eta_{\Lambda_{d-1}}$ and η_{d-1} of $\mathcal{M}_{\Lambda_{d-1}}$ and \mathcal{M}_{d-1} are related by the factor ψ .

Due to the potential non-conformity of the mortar meshes with respect to the adjacent meshes used for the discretization of the flow equations, we need to project data from and to the mortar grid. In particular, let us denote by $\Pi_{\Lambda_d}^{\iota}$ the projection of the mortar variable onto a discrete entity ι of the adjacent discretizations, and by Π_v^E the projections of a variable v defined on an adjacent subdomain onto the space of piecewise constants (per grid element) on \mathcal{M}_{Λ_d} . For example, $\Pi_{\Lambda_d}^{\sigma}$ is the projection of the mortar variable onto the face $\sigma \in \mathcal{S}_{d+1,c}$, and $\Pi_{h_d}^E$ is the projection of the hydraulic head onto the element $E \in \mathcal{M}_{\Lambda_d}$. Since we only consider projections into spaces of piecewise constants, they can be constructed by computing the overlapping regions between elements of the different discretizations and integrating over them.

Discrete flux expressions on coupling faces. With the projections defined, the interface fluxes on coupling faces $\sigma \in \mathcal{S}_{d,c}$, embedded in the control volume $K \in \mathcal{K}_d$, are simply given by the projection of the corresponding mortar variable:

$$F_K^{\sigma} = \Pi_{\Lambda_{d-1}}^{\sigma}. \quad (22)$$

Interface conditions. Recall that, depending on the permeability contrast between the adjacent subdomains, two types of interface conditions are considered, stated in eqs. (11a) and (11b). Therefore, let us partition the elements of the mortar discretization \mathcal{M}_{Λ_d} into the sets $\mathcal{E}_{d,\mathcal{H}}$ and $\mathcal{E}_{d,\mathcal{B}}$, which collect the elements that live on interfaces on which the conditions (11b) and (11a) should hold, respectively. The interface conditions are then enforced by solving

$$\Lambda_E + \Pi_{|\epsilon_{d+1}|}^E \Pi_{\Psi_d}^E = 0, \quad \text{on } E \in \mathcal{E}_{d,\mathcal{B}}, \quad (23a)$$

$$\Pi_{h_{d+1}}^E - \Pi_{h_d}^E = 0, \quad \text{on } E \in \mathcal{E}_{d,\mathcal{H}}, \quad (23b)$$

where we have introduced

$$\Psi_d = \mathbf{n}^T \mathbf{K}_d \mathbf{n} \frac{h_d - \Pi_{h_{d+1}}^E}{L_d} \quad (24)$$

for the sake of readability. Note that eq. (23b) is independent of the mortar variable, which means that the associated rows of the linear system contain zeros on the main diagonal, and only contain values in the coupling blocks. Therefore, when using the conditions (1c), we have experienced that the system matrices become singular when $\psi < 1$, which seems to cause the system to be overconstrained. This is in agreement with the analysis provided in Wohlmuth (2011), where Lagrange multiplier approaches are investigated in the context of contact mechanics. They show that for piecewise constant mortars, the system is unstable also for $\psi = 1$, but one possible remedy is to use coarser meshes for the mortar discretization. The case of $\psi = 1$ is briefly discussed in the numerical examples given in section 5, but in general we choose $\psi > 1$ whenever the conditions (23b) are used.

5. Numerical experiments

Ideally, a numerical method should be both efficient and accurate in order to be useful, for instance, in the design process of a geotechnical engineering application. Therefore, the test cases presented in the sequel aim at comparing the above-mentioned schemes in terms of accuracy and efficiency. We start with an investigation of the convergence behavior of the schemes against an analytical solution in section 5.1. Similar investigations have been the subject of various works in the literature, where several authors (see e.g. Sandve et al. (2012); Ahmed et al. (2015, 2017); Gläser et al. (2017)) used the analytical solution proposed in Hægland et al. (2009), although originally derived for the equi-dimensional model problem. Consequently, it was observed that convergence is lost when the size of the cells of the bulk discretization approaches the aperture of the fracture, and an irreducible error remains. This is expected as the mixed-dimensional formulation is an approximation to the equi-dimensional problem. However, it is questionable if that irreducible error provides a good measure of the modelling error introduced by the dimension reduction of the fracture. In Gläser et al. (2017) it was observed that convergence can be maintained up to smaller cell sizes if the volume error is ruled out, while Gläser (2020) report that the same can be achieved by integrating the source term in the bulk elements adjacent to the fracture only over the region that is not occupied by the fracture in the equi-dimensional setting. Such issues seem to have little relevance to applications where the models could be applied to. Moreover, the analytical solution is defined such that no jump in hydraulic head occurs across the fracture, independent of the chosen permeability contrast, which does not allow for a statement to be made whether or not a model can be applied to low-permeable fractures. A mixed-dimensional analytical solution is reported, for instance, in e.g. Antonietti et al. (2016), which overcomes the issue with integration of the source term, but it also does not feature a jump in the hydraulic head, which could appear in the case of low-permeable fractures.

In this work, we want to propose an analytical solution to the mixed-dimensional problem, in which the hydraulic head is discontinuous across the fracture for small values of the fracture permeability, but approaches continuity for high fracture permeabilities or small aperture values. This is subject of section 5.1, while in section 5.2 we want to investigate the errors introduced by the dimension reduction of the fracture using discrete reference solutions obtained on equi-dimensional discretizations. Therein, we also study the performance of the schemes for anisotropic permeability tensors in the bulk medium. In section 5.3, we lay special focus on the hydraulic head and fluxes at the bulk-fracture interface, and compare the EBOX-DFM and the EBOX-MORTAR-DFM schemes when the conditions eq. (11b) are used. Finally, we apply the schemes to two- and three-dimensional benchmark cases in section 5.4 and section 5.5, where, apart from the numerical results, we compare the different schemes in terms of computational efficiency.

5.1. Case 1: analytical reference solution

Let us consider the unit square $\Omega = \Omega_2 = (-0.5, 0.5) \times (-0.5, 0.5)$ to describe a porous medium that is intersected by a single horizontal and lower-dimensional fracture $\Omega_1 = (-0.5, 0.5) \times \{0\}$. The lower and upper parts of Ω_2 , that are separated by the fracture, are denoted by Ω_2^1 and Ω_2^2 , respectively. The permeability of the bulk domain is $\mathbf{K}_2 = \mathbf{I}$ m/s and that of the fracture $\mathbf{K}_1 = k \mathbf{I}$ m/s. On this setting, let us define with

$$\Delta H = \frac{a}{k} (x + 0.5)^2 \quad (25)$$

a jump in hydraulic head across the fracture, for which we observe that $\Delta H \rightarrow 0$ for $a/k \rightarrow 0$ and $x \in [-0.5, 0.5]$. The proposed analytical solution, denoted by h_d^* , reads:

$$h_2^*(x, y) = x^3 + y^3 + y(x + 0.5)^2 - \frac{\Delta H}{2}, \quad \text{for } (x, y) \in \Omega_2^1, \quad (26a)$$

$$h_2^*(x, y) = x^3 + y^3 + y(x + 0.5)^2 + \frac{\Delta H}{2}, \quad \text{for } (x, y) \in \Omega_2^2, \quad (26b)$$

$$h_1^*(x, y) = x^3, \quad \text{for } (x, y) \in \Omega_1, \quad (26c)$$

with the source terms

$$q_2(x, y) = -6x - 8y + \frac{a}{k}, \quad \text{for } (x, y) \in \Omega_2^1, \quad (27a)$$

$$q_2(x, y) = -6x - 8y - \frac{a}{k}, \quad \text{for } (x, y) \in \Omega_2^2, \quad (27b)$$

$$q_1(x, y) = -6kx, \quad \text{for } (x, y) \in \Omega_1. \quad (27c)$$

In fig. 5, the solution is visualized for $a = 1 \cdot 10^{-4}$ m and $k \in \{1 \cdot 10^{-4}, 1 \cdot 10^4\}$, which are the two

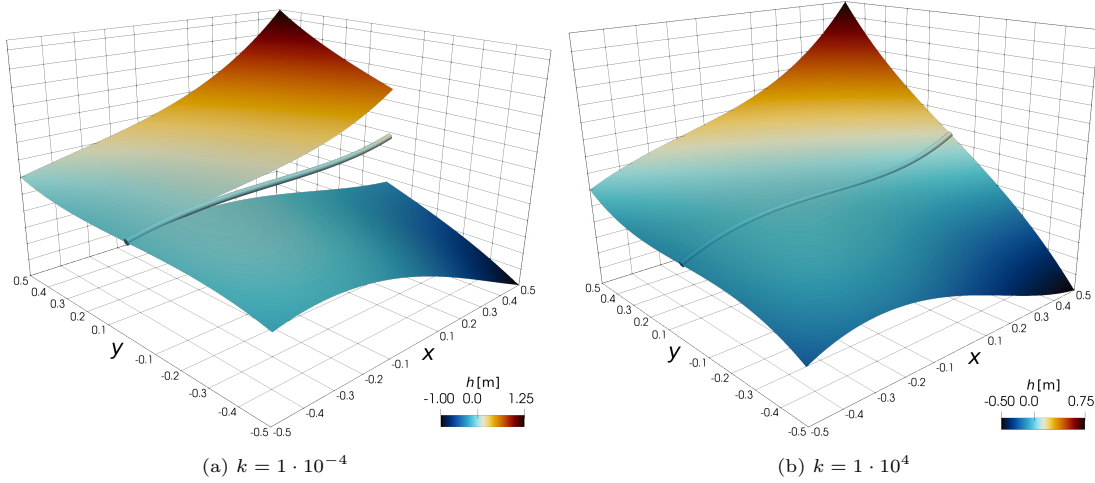


Figure 5: **Case 1 - discrete solutions.** Depicted are the discrete solutions obtained with the EBOX-DFM scheme on the finest grid of the convergence test. The solution in the fracture is illustrated by the tube at $y = 0$.

cases that we consider in the analysis. We use Dirichlet boundary conditions on all boundaries and set $\mathcal{S}_{d,c} \equiv \mathcal{S}_{d,B}$, that is, the conditions (11a) are enforced on all coupling faces. For the EBOX-MORTAR-DFM scheme we use $\psi = \{0.5, 1.2, 2.0\}$, that is, we consider the case that the mortar grid cells coincide with the coupling sub-control volume faces of the bulk discretization, the case of a non-conforming mortar grid, and a mortar grid whose elements contain exactly four bulk sub-control volume faces. For the quantification of the errors of the discrete solution with respect to the analytical solution we use the norm

$$\varepsilon_{h_2}^i = \frac{\sqrt{\sum_{E \in \mathcal{M}_2^i} \int_E (h - h^*)^2}}{\sqrt{\sum_{E \in \mathcal{M}_2^m} \int_E (h^*)^2}} \quad (28)$$

for the hydraulic head in the bulk medium, and for the bulk-fracture transfer fluxes we use

$$\varepsilon_{\lambda}^i = \frac{\sqrt{\sum_{\sigma \in \mathcal{S}_{2,c}^i} \int_{\sigma} (\lambda - \lambda^*)^2}}{\sqrt{\sum_{\sigma \in \mathcal{S}_{2,c}^m} \int_{\sigma} (\lambda^*)^2}}, \quad (29)$$

where we have introduced $\lambda = \mathbf{q}_2 \cdot \mathbf{n}|_{\gamma_1}$ for the sake of readability. In the above norms, i is the refinement index, $0 < i \leq m$, and \mathcal{M}_2^i denotes the corresponding mesh of the bulk medium. The analysis is performed on structured rectangular grids, and therefore, we do not consider the MPFA-DFM scheme in the discussion as it reduces to the TPFA-DFM scheme on such settings, yielding the exact same results.

Figure 6 shows the plots of the errors over grid refinement, where second-order convergence is observed in h_2 for the vertex-centered EBOX-DFM and EBOX-MORTAR-DFM schemes, both for a

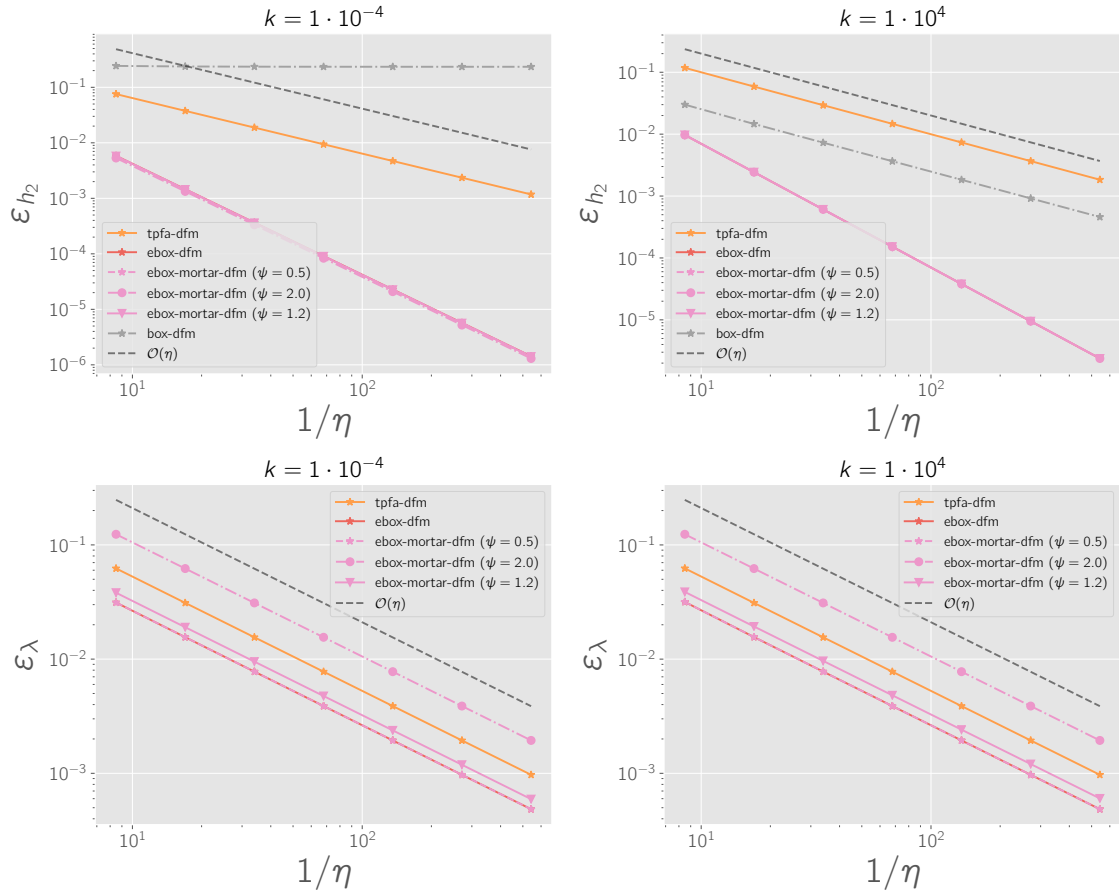


Figure 6: **Case 1 - errors over grid refinement:** the errors in h_2 and the mass transfer λ are plotted over grid refinement. The x-axis shows the inverse of the discretization length η and the left and right columns depict the results for $k = 1 \cdot 10^{-4}$ and $k = 1 \cdot 10^4$, respectively.

highly-permeable and a low-permeable fracture. Furthermore, the errors and convergence behavior of the EBOX-MORTAR-DFM scheme seems to be independent of the grid ratio ψ . In particular, almost the same errors and rates are observed for the case of non-matching mortar grids ($\psi = 1.2$). In contrast to that, first-order convergence is observed for the TPFA-DFM scheme. Note that second-order convergence would be seen if a norm based on point-wise error computations in the grid element centers was used (Sandve et al., 2012; Ahmed et al., 2015; Gläser et al., 2017), however, a benefit of the vertex-centered schemes is that they allow for a straightforward interpolation of the hydraulic head within the entire domain. Finally, first-order convergence is observed for the BOX-DFM scheme in the case of $k = 1 \cdot 10^4$, while convergence is lost for the low-permeable fracture as a consequence of the assumption of continuity of the hydraulic head.

The interface flux λ converges with first order for all schemes that allow for its evaluation, and it can be seen that this holds again for all considered values of ψ . As expected, higher errors in λ are observed for coarser mortar discretizations, while the convergence rates seem not to be affected by the choice of ψ . Please note that results for the BOX-DFM scheme are not shown in the plots for ε_λ , as the scheme does not allow for an evaluation of the interface flux, which also does not appear in its formulation.

5.2. Case 2: discrete reference solution

As in the previous test case, we consider the domain $\Omega_2 = (-0.5, 0.5) \times (-0.5, 0.5)$ for the bulk medium, and take into account three different fracture configurations \mathcal{F}_k , $k \in \{1, 2, 3\}$, composed

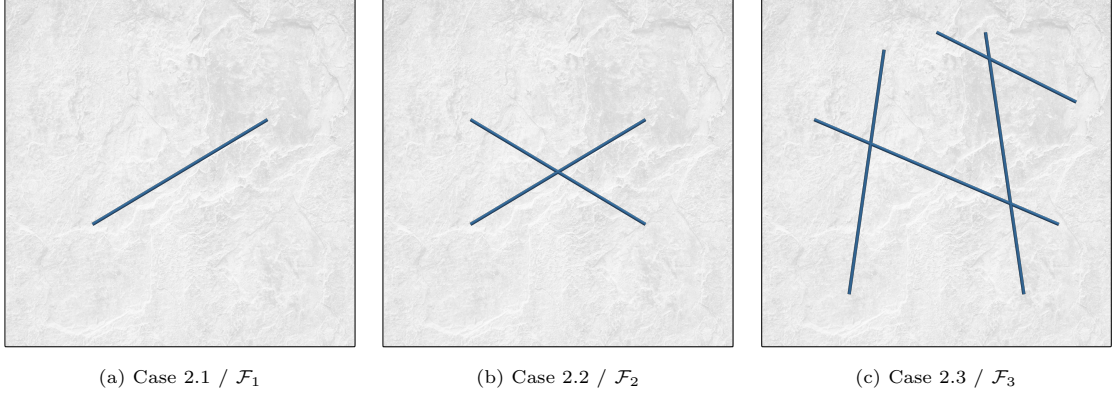


Figure 7: **Case 2 - fracture networks**: the figure depicts the three different fracture configurations, illustrated by the blue lines, that are investigated in the convergence tests against equi-dimensional reference solutions.

of individual fractures f such that $\mathcal{F}_k = \bigcup_{f \in \mathcal{F}_k} f$. An illustration of the different networks can be found in fig. 7. The permeabilities in the subdomains are given by (in m/s)

$$\mathbf{K}_b = \mathbf{K}_2 = \mathbf{R}(\Theta)^{-1} \begin{pmatrix} 1 & 0 \\ 0 & 1/5 \end{pmatrix} \mathbf{R}(\Theta), \quad \mathbf{K}_f = \mathbf{K}_1 = k \mathbf{I}, \quad (30)$$

where \mathbf{R} is the two-dimensional rotation matrix in clockwise direction around the angle Θ , and we consider both highly-permeable as well as blocking fractures by choosing k accordingly. An aperture of $a = 2 \cdot 10^{-3}$ m is used for all fractures and Dirichlet boundary conditions are applied on the entire outer boundary, evaluated after

$$h_2^D = \left(1 - (x - 0.5)^2\right) (1 - \cos(\pi y)), \quad \text{for } (x, y) \in \Gamma_2. \quad (31)$$

Discrete error norms. For each of the three fracture networks, we want to study the convergence behaviour of the different mixed-dimensional schemes against equi-dimensional reference solutions, which we obtain with the MPFA scheme, for different combinations of k and Θ . To this end, we create equi-dimensional discretizations of the domain geometries by describing each fracture as a rectangle with a thickness equal to the aperture a . The equi-dimensional fracture domain Ω_f is then obtained by computing the union of all fractures. Let us denote the equi-dimensional discretizations by \mathcal{M}^{eq} and the corresponding numerical solution by h^{eq} . We then extract the sub-meshes of \mathcal{M}^{eq} that describe the bulk medium and the fractures, which we denote here by $\mathcal{M}_b^{\text{eq}}$ and $\mathcal{M}_f^{\text{eq}}$, respectively. Let \mathcal{M}_2^i , $0 \leq i \leq 5$, be the i -th refinement of the discretization of the bulk domain in the mixed-dimensional setting with the associated numerical solution h_2^i . The error of h_2^i with respect to the reference solution is evaluated after

$$\varepsilon_{h_2}^i = \frac{\sqrt{\sum_{E \in \mathcal{M}_b^{\text{eq}}} \left(\Pi_{h_2^i}^E - h_E^{\text{eq}}\right)^2 |E|}}{\sqrt{\sum_{E \in \mathcal{M}_b^{\text{eq}}} \left(h_E^{\text{eq}}\right)^2 |E|}}, \quad (32)$$

where $\Pi_{h_2^i}^E$ is the L2-projection of h_2^i onto the element $E \in \mathcal{M}_b^{\text{eq}}$. In order to evaluate the error in h_1^i , we generate one-dimensional reference solutions h_f^* by averaging and projecting the equi-dimensional solution onto fine discretizations of the individual fractures. These are denoted by \mathcal{M}_f , $f \in \mathcal{F}_k$, and allow for the computation of the error in h_1 for the i -th refinement and the k -th fracture network after the following expression:

$$\varepsilon_{h_1}^i = \frac{\sum_{f \in \mathcal{F}_k} \sqrt{\sum_{E \in \mathcal{M}_f} \left(\Pi_{h_1^i}^E - h_E^*\right)^2 |E|}}{\sum_{f \in \mathcal{F}_k} \sqrt{\sum_{E \in \mathcal{M}_f} \left(h_E^*\right)^2 |E|}}. \quad (33)$$

Table 1: **Case 2 - meshes used in the convergence tests.** Discretization lengths used for the equi-dimensional reference grid, expressed as multiples of the fracture aperture a . Additionally, the resulting number of elements are given for both the reference and the coarsest and finest mixed-dimensional meshes.

	$ \mathcal{M}^{\text{eq}} $	$ \mathcal{M}_2^0 $	$ \mathcal{M}_1^0 $	$ \mathcal{M}_2^5 $	$ \mathcal{M}_1^5 $
\mathcal{F}_1	351 768	172	24	176 128	768
\mathcal{F}_2	1 089 484	420	48	430 080	1536
\mathcal{F}_3	3 839 860	1386	112	1 419 264	3584

Discretization choices. We use triangular grids in all simulations, and in order to reduce the cost for the computation of the reference solution, we use locally refined meshes towards the fractures, where we choose a characteristic discretization length $\eta_f^{\text{eq}} = a/6$ in and around the fractures, and use $\eta_\Gamma^{\text{eq}} = 5a$ at the exterior domain boundary. For the mixed-dimensional discretizations, we generate initial meshes using $\eta_f = 75\eta_f^{\text{eq}}$, and $\eta_\Gamma = \eta_f\eta_\Gamma^{\text{eq}}/\eta_f^{\text{eq}}$ in order to have the same coarsening ratio towards the boundaries as in the reference grid. All subsequent refinements are obtained by subdivision of the grid elements. This strategy results in meshes as listed in table 1, where the number of elements in the reference grid as well as the coarsest and finest mixed-dimensional grids are given. As can be seen, the ratio $|\mathcal{M}^{\text{eq}}|/|\mathcal{M}_2^5|$ is similar for all fracture networks, ranging from 2 to 2.7. For the discretization of the mortar domain we use $\psi = 1.2$, and as in the previous convergence test, we set $\mathcal{S}_{d,c} \equiv \mathcal{S}_{d,b}$ in all simulations. Please note that while on the structured grids used in the previous test case the ratio ψ between the discretization lengths used in the mortar and fracture domains was identical along the entire fracture, this is no longer the case for the unstructured grids used in this example. Here, ψ refers to the ratio of the characteristic lengths used to generate the meshes with the mesh generation tool Gmsh (Geuzaine & Remacle, 2009), but that does not mean that this ratio is fulfilled for all elements of the grids. The same also holds for the grids used in sections 5.3 and 5.4.

The convergence tests are carried out for $k \in \{1 \cdot 10^{-4}, 1 \cdot 10^4\}$ and $\Theta \in \{0, \pi/4\}$, and all errors and rates are listed in the appendix in tables 5 to 7, of which we will discuss a selection in the subsequent paragraphs. In addition, we present results obtained from further sets of simulations targeted at investigating the dependency of the errors on a wider range of k and Θ . While using the same reference grid, we use mixed-dimensional discretizations that are not obtained by refinement, in contrast to the convergence tests, but instead, we generate triangulations by choosing η_f as in \mathcal{M}_1^5 . Table 2 lists the meshes used in those simulations, and it can be seen that it is $|\mathcal{M}^{\text{eq}}|/|\mathcal{M}_2| \approx 5.5$ for all fracture networks.

Table 2: **Case 2 - meshes used in the additional simulations.** Number of elements in the mixed-dimensional discretizations used to investigate the dependency of the errors on k and Θ .

	\mathcal{F}_1	\mathcal{F}_2	\mathcal{F}_3
$ \mathcal{M}_2 $	62 254	196 476	699 682
$ \mathcal{M}_1 $	747	1496	3428

Fracture network \mathcal{F}_1 . As illustrated in fig. 7a, this setting consists of a single fracture placed in the center of the domain. The distributions of the hydraulic head for $\Theta = 0$ and both fracture permeabilities are depicted in fig. 8, which also shows the relative errors plotted over grid refinement. One expected observation we make, given that unstructured meshes and anisotropic permeabilities are used, is that the TPFA-DFM scheme does not converge in any of the considered quantities and for none of the considered parameter choices. The error only slightly decays upon refinement, and relative errors in the order of 10% remain on the finest grid. In contrast to that, we observe that h_2 converges with approximately first order for all remaining schemes in the case of $k = 1 \cdot 10^4$, while the rates slightly decay upon the last refinement for $k = 1 \cdot 10^{-4}$ (see fig. 8e). However, the errors

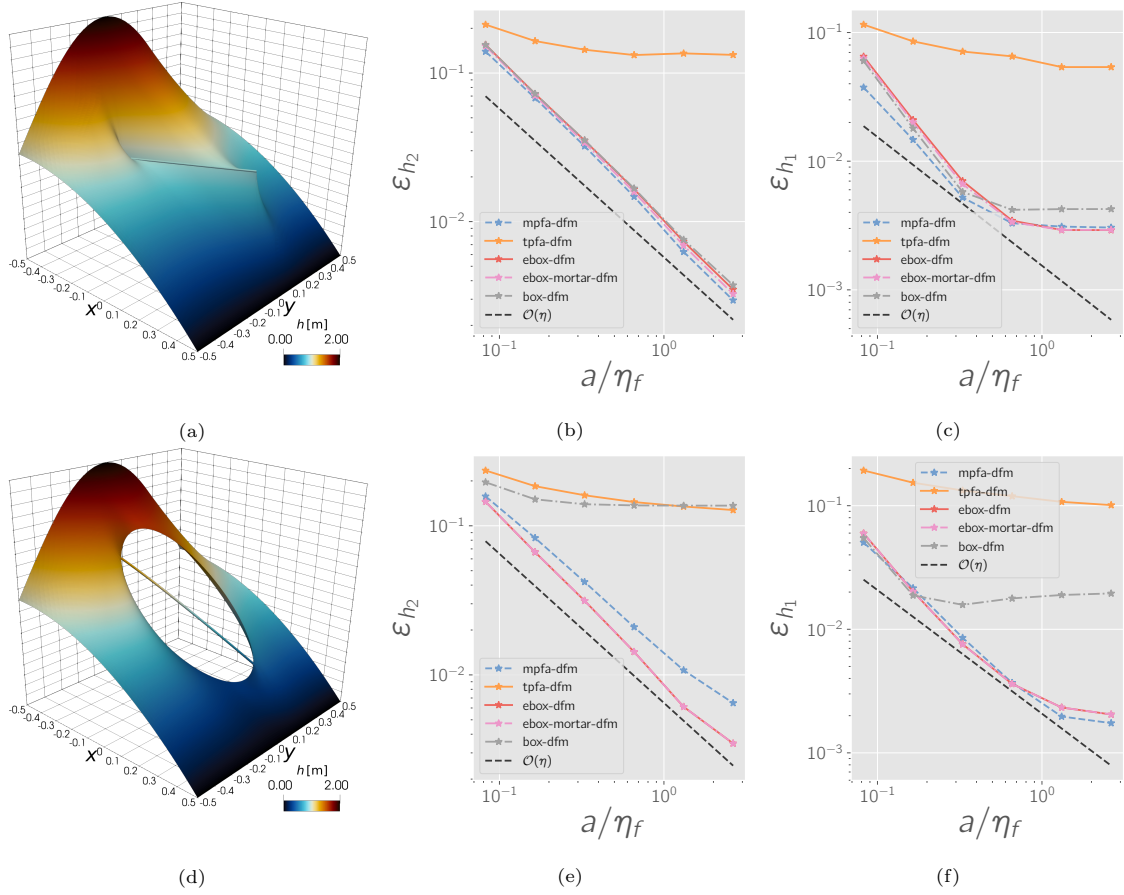


Figure 8: **Case 2.1 - results for $\Theta = 0$** . The upper row and lower row show the results for $k = 1 \cdot 10^4$ and $k = 1 \cdot 10^{-4}$, respectively. The left column depicts the distributions of the hydraulic heads in the domain, obtained with the EBOX-DFM scheme on the finest grid, while the middle and right columns show the errors in h_2 and h_1 plotted over grid refinement.

drop below 1% after the third refinement in both cases. It is also noteworthy that for $k = 1 \cdot 10^4$, the MPFA-DFM, EBOX-DFM and EBOX-MORTAR-DFM schemes lead to very similar errors in each refinement, while for $k = 1 \cdot 10^{-4}$, we see that the vertex-centered schemes produce slightly smaller errors. Apart from that, only very minor differences in errors are observed between the EBOX-DFM and the EBOX-MORTAR-DFM schemes, despite the more than two times coarser discretization of the interface fluxes in the latter. Note that second-order convergence cannot be expected in this case due to the projections into the space of piecewise constants on the reference grid.

The plots of ε_{h_1} , given in figs. 8c and 8f, show that the convergence rates deteriorate when the discretization length around the fracture η_f approaches the aperture a . As mentioned in the introduction to this section, this is expected since the mixed-dimensional model is an approximation to the equi-dimensional problem. However, rather small relative errors below 0.5% are observed on the finest grid. Qualitatively similar results were also observed for $\Theta = \pi/4$, which are given in tables 7 and 8, with the main difference being that smaller errors are obtained with the BOX-DFM scheme for $k = 1 \cdot 10^{-4}$. This stems from the fact that for $\Theta = \pi/4$ the jump in hydraulic head across the fracture is significantly smaller for the chosen fracture orientation and boundary conditions.

Figure 9 depicts the results obtained from a set of additional simulations carried out on the mesh as specified in table 2. Again, a very similar performance of the MPFA-DFM, EBOX-DFM and

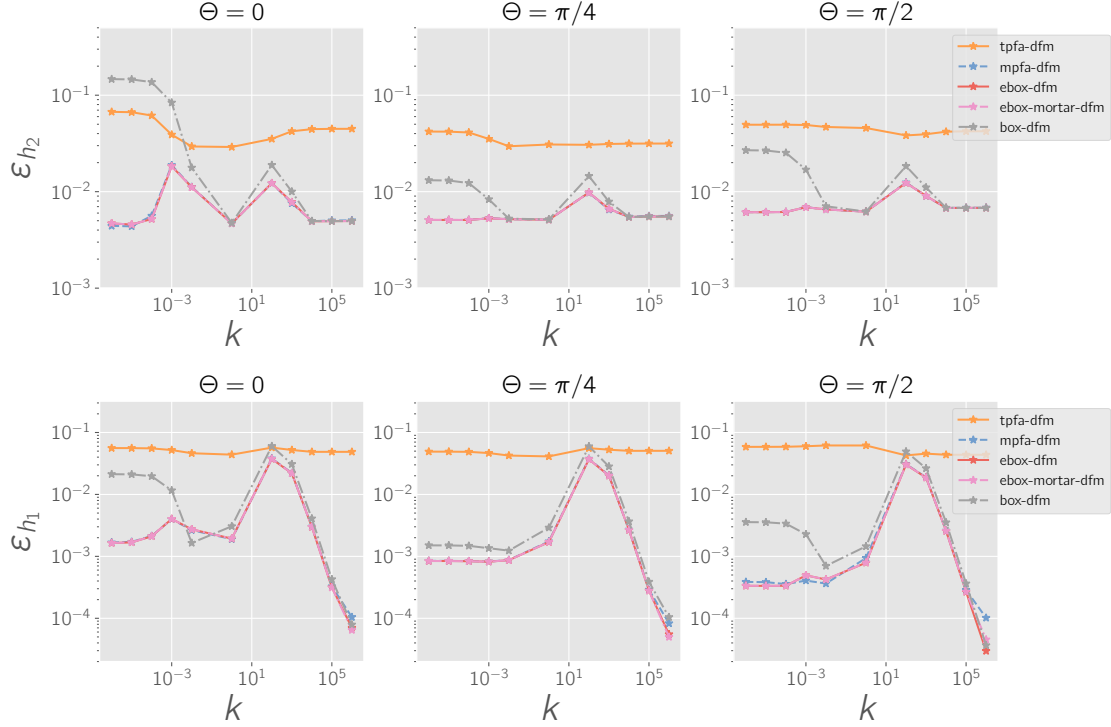


Figure 9: **Case 2.1 - error over k** . The errors in h_2 and h_1 , obtained on the meshes as specified in table 2, are plotted over k for various values of the permeability angle Θ .

EBOX-MORTAR-DFM schemes is observed, for which the error in h_2 lies between 0.5% and 2% for all values of k and Θ . As mentioned, the jump in h_2 across the fracture is largest for $\Theta = 0$. In this case, it can be seen from fig. 9, that the error is largest for moderate permeability contrasts, as for $k = 1 \cdot 10^{-3}$ the observed error is about three times higher as for $k \leq 1 \cdot 10^{-4}$. For the TPGA-DFM scheme, the errors are about half of those observed on the finest grid of the convergence test (see fig. 8b). This seems to be related to the differences in the grids used, and indicates that the grids obtained by refinement have properties that promote the inconsistency of the scheme. Moreover, fig. 9 illustrates the dependency of the error on k for the BOX-DFM scheme. While for large values of k the errors are similar to those obtained with the EBOX-DFM scheme, larger errors are observed for decreasing k , leading to $\varepsilon_{h_2} > 10\%$ for $k < 1 \cdot 10^{-3}$ and $\Theta = 0$. As mentioned, the jump in h_2 across the fracture is smaller for $\Theta \in \{\pi/4, \pi/2\}$, which explains the smaller errors in h_2 for low fracture permeabilities in these cases. Furthermore, it can be seen that the error in h_1 shows the highest values for moderate permeability contrasts and $k > 1$, while for $k < 1$, no strong fluctuations of ε_{h_1} can be observed. Most notably, the error strongly decreases for $k > 1 \cdot 10^3$.

Fracture network \mathcal{F}_2 . The geometric complexity is increased with this fracture network as it contains an intersection of two fractures (see fig. 7b). In the mixed-dimensional model, we treat 0-dimensional fracture intersections by the conditions (10), that is, the intersection region is not described by an individual subdomain. However, in the equi-dimensional discretization, the intersection region is resolved and populated with grid elements, and therefore, we assign the permeability \mathbf{K}_f to those elements in order to minimize deviations in the setup.

In the following we want to focus on the discussion of the results for $\Theta = \pi/4$, which are again qualitatively similar to those obtained for $\Theta = 0$ and which can be found in tables 5 and 6. The solution and plots of the error norms can be seen in fig. 10, which shows that very similar errors in h_2 , both qualitatively and quantitatively, are obtained when compared to those for \mathcal{F}_1 .

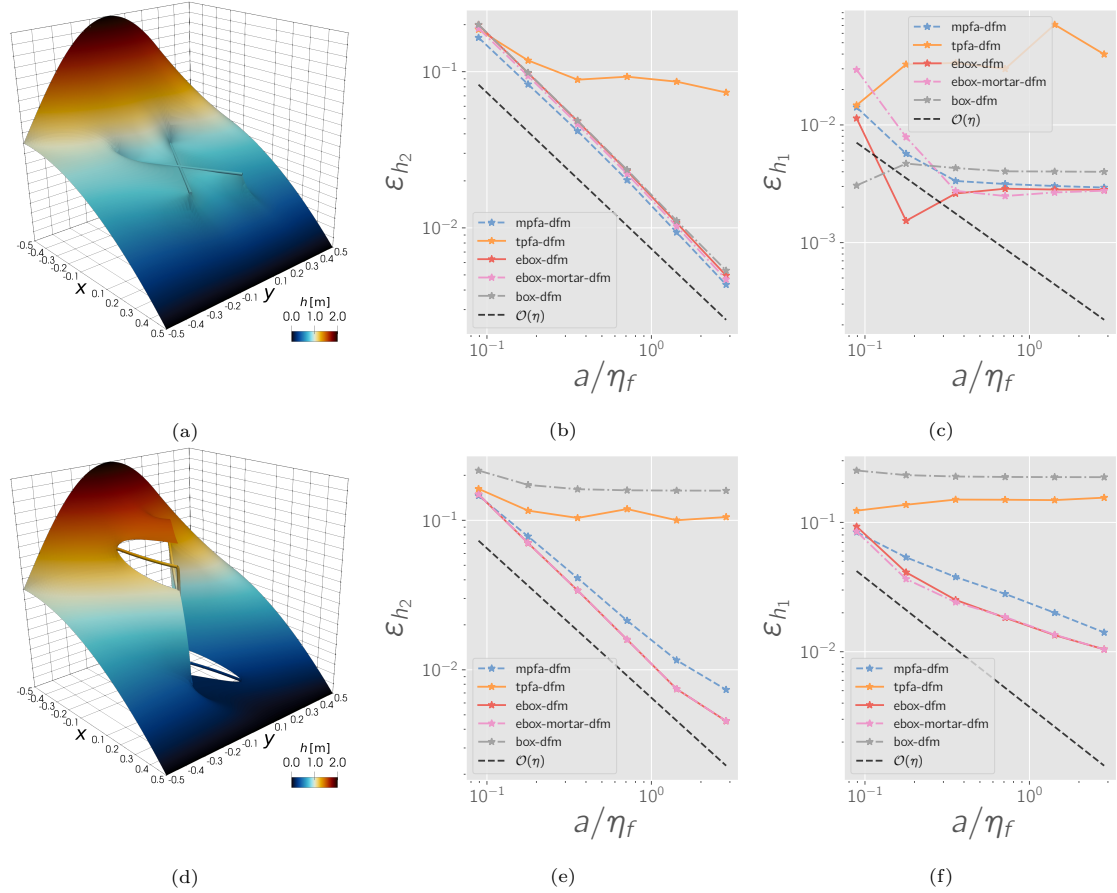


Figure 10: **Case 2.2 - results for $\Theta = \pi/4$.** The upper row and lower row show the results for $k = 1 \cdot 10^4$ and $k = 1 \cdot 10^{-4}$, respectively. The left column depicts the distributions of the hydraulic heads in the domain, obtained with the EBOX-DFM scheme on the finest grid, while the middle and right columns show the errors in h_2 and h_1 plotted over grid refinement.

Concerning h_1 , we again observe that convergence is lost after a few refinements, leading to very similar irreducible relative errors after the last refinement. Noticeable differences to the results obtained on \mathcal{F}_1 can be seen for h_1 and $k = 1 \cdot 10^{-4}$, where lower convergence rates are obtained already after the first refinement. This is probably related to the fact that in the presence of fracture intersections in low-permeable fracture networks, complex distributions of the hydraulic head within the intersection region might develop, which are not captured by the mixed-dimensional model. Nevertheless, the relative error is reduced to $\approx 1\%$ in the last refinement, while errors below 1% are again reached for h_2 .

Figure 11 depicts the errors in h_2 and h_1 obtained from additional simulations using a mixed-dimensional discretization as given in table 2. As for \mathcal{F}_1 (see fig. 9), the error seems to be largest for moderate permeability contrasts, while on this network, we observe less dependency on the permeability angle Θ . This can be explained by the fact that the jump in hydraulic head across the fractures is less dependent on Θ in the case of \mathcal{F}_2 , where there is always a fracture oriented in orthogonal direction to the flow field. Consequently, significant errors can be seen for the BOX-DFM scheme and low permeabilities for all values of Θ . A noteworthy difference to the results of \mathcal{F}_1 is that the errors in h_1 are about an order of magnitude larger for $k < 1 \cdot 10^{-3}$, which reflects the lower convergence rates observed in this case, as was discussed earlier.

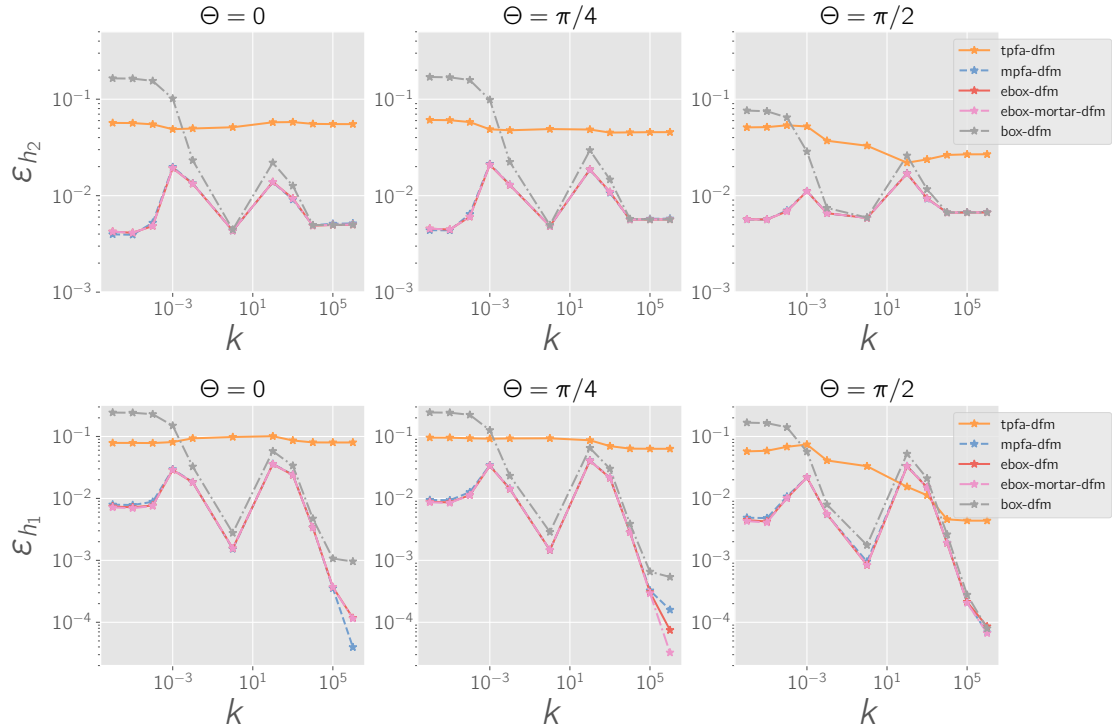


Figure 11: **Case 2.2 - error over k** . The errors in h_2 and h_1 , obtained on the meshes as specified in table 2, are plotted over k for various values of the permeability angle Θ .

Fracture network \mathcal{F}_3 . This is the most complex of the networks considered in this test case, consisting of four intersecting fractures. In the discussion, we want to focus again on the results obtained for $\Theta = \pi/4$, which are depicted in fig. 12b, while those for $\Theta = 0$ can be found in tables 5 and 6 in the appendix. In contrast to the previous two networks, the rate of convergence in h_2 , for $k = 1 \cdot 10^4$, starts to decrease upon the last refinement. Moreover, only a small reduction of the error ε_{h_1} in the fractures is observed, which stagnates at $\approx 1\%$.

However, despite the significantly increased complexity, the errors obtained on the finest grid are comparable to those obtained on \mathcal{F}_2 (see fig. 10), which can also be seen in fig. 11, where the errors for a wider range of values for k , computed on the mesh listed in table 2, is shown. Both qualitatively and quantitatively, very similar results to those obtained on \mathcal{F}_2 (see fig. 9) are observed, while the main difference is that we do not see an increase in ε_{h_1} for moderately low-permeable fractures on \mathcal{F}_3 .

Summary. The results show that the EBOX-DFM and EBOX-MORTAR-DFM schemes, being applicable to both low- and highly-permeable fractures and arbitrary bulk permeability angles Θ , lead to similar or slightly lower errors as the MPFA-DFM scheme. Convergence in h_2 was maintained over all grid refinements, while the errors in h_1 showed to stagnate when the discretization length approaches the aperture. With increasing complexity of the fracture network, this stagnation seemed to occur earlier in the refinement cycle, at least for $k = 1 \cdot 10^4$, while for $k = 1 \cdot 10^{-4}$, lower convergence rates were observed already in the first refinements. This is probably due to the complex jumps in hydraulic head that develop across intersecting fractures, which the mixed-dimensional model struggles to capture.

The BOX-DFM scheme leads to comparable errors for large values of k , for which its model assumptions are fulfilled. However, for moderate permeability contrasts it led to larger errors

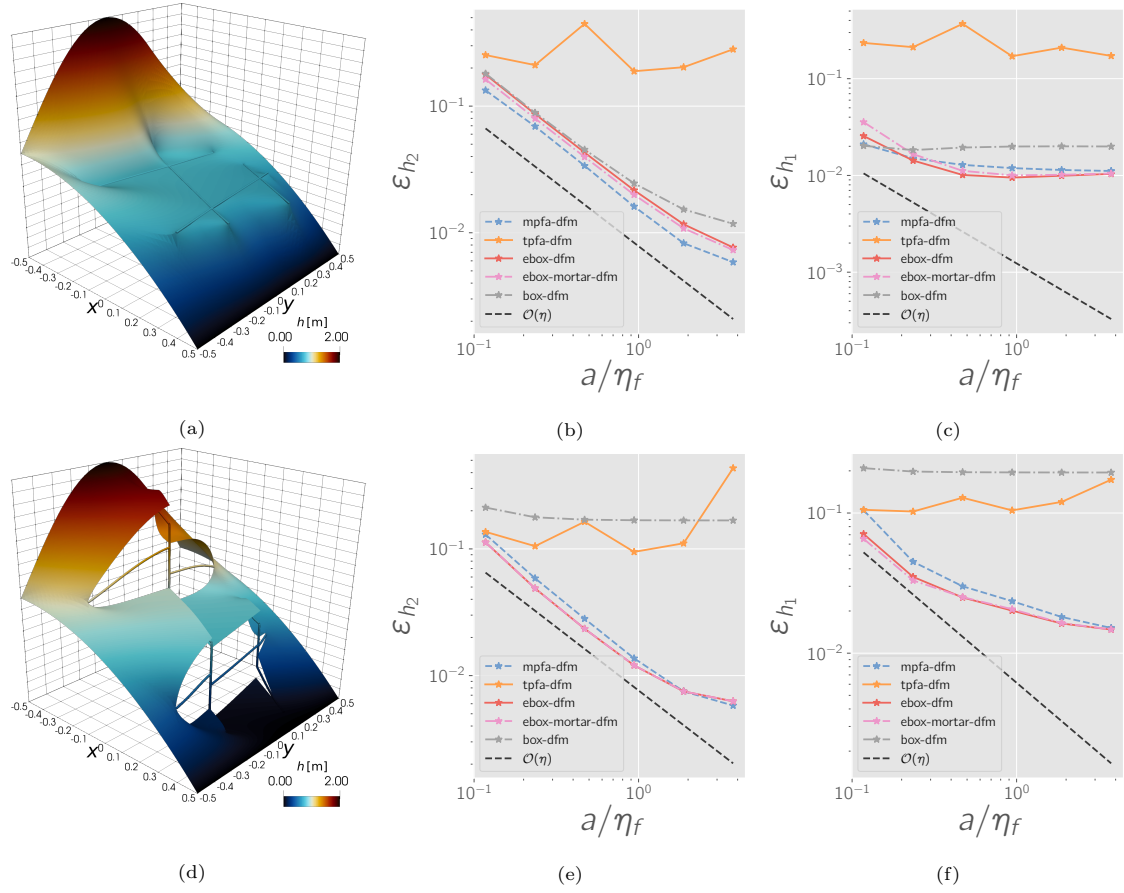


Figure 12: **Case 2.3 - results for $\Theta = \pi/4$.** The upper row and lower row show the results for $k = 1 \cdot 10^4$ and $k = 1 \cdot 10^{-4}$, respectively. The left column depicts the distributions of the hydraulic heads in the domain, obtained with the EBOX-DFM scheme on the finest grid, while the middle and right columns show the errors in h_2 and h_1 plotted over grid refinement.

when compared to the MPFA-DFM or the other vertex-centered schemes, and for $k \leq 1 \cdot 10^{-3}$, errors above 10% were observed. Despite the similarity in the results between the MPFA-DFM and the EBOX-DFM and EBOX-MORTAR-DFM schemes, the vertex-centered schemes use much less degrees of freedom on unstructured grids and lead to smaller stencils. This issue will be investigated in more detail in sections 5.4 and 5.5.

5.3. Case 3: interface flux and hydraulic head

This test case focuses on the vertex-centered EBOX-DFM and EBOX-MORTAR-DFM schemes, and in particular, on the bulk-fracture interface flux and hydraulic head. To this end, we again consider a unit square bulk domain, and reuse eq. (31) as Dirichlet boundary conditions on the entire bulk domain boundary. A single fracture is placed in the domain, defined as the connecting segment between the points $(-0.15, 0.35)$ and $(0.2, -0.35)$. As in the previous test case, we consider an aperture of $a = 2 \cdot 10^{-3}$ and generate an equi-dimensional discretization of the domain following the procedure described in section 5.2, on which a reference solution is computed with the MPFA scheme. A rather coarse mixed-dimensional discretization is used, consisting of 28 266 triangular and 235 line elements, while the reference grid contains 532 384 triangular elements. We are particularly interested in differences among the two schemes in fulfilling the conditions (11b) at interfaces to highly-permeable or open fractures. Therefore, we consider the permeabilities used in section 5.2 with $k = 1 \cdot 10^4$.

Let us first look at the results for the case of $\mathcal{S}_{d,c} \equiv \mathcal{S}_{d,B}$, that is, using the conditions (11a) at

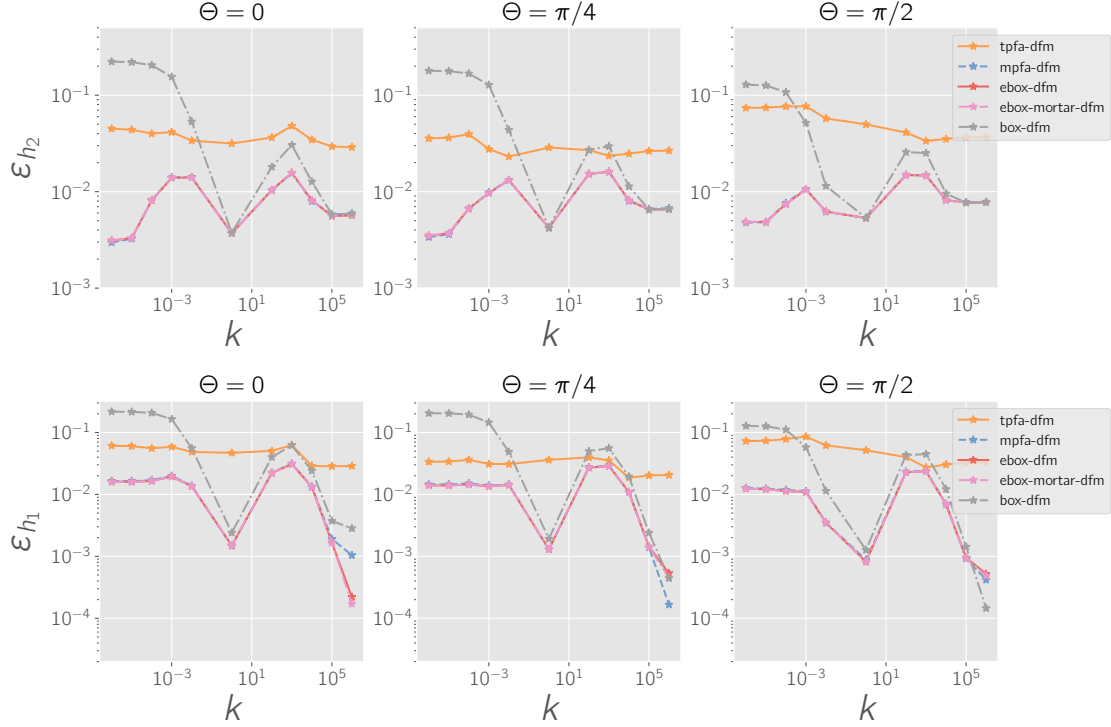


Figure 13: **Case 2.3 - error over k** . The errors in h_2 and h_1 , obtained on the meshes as specified in table 2, are plotted over k for various values of the permeability angle Θ .

the bulk-fracture interface. Figure 14 shows the transfer flux λ , the term $(\mathbf{K}\nabla h_2) \cdot \mathbf{n}|_{\gamma_1}$ and the hydraulic heads h_2 and h_1 in the bulk medium and the fractures, plotted along the interface γ_1 . Recall that for immersed fractures it is $m_1^{i,j} = 2$, that is, the interface $\gamma_1^{i,j}$ consists of both sides of the fracture on which fluxes and hydraulic heads might have different values. Therefore, the plots in fig. 14 are restricted to the lower left fracture side on which $\mathbf{e}_1 \cdot \mathbf{n}|_{\gamma_1} > 0$, $\mathbf{e}_1 = (1, 0)^T$, holds for the outer normal vector.

From the upper row of fig. 14 it can be seen that the transfer fluxes produced by the EBOX-DFM and the EBOX-MORTAR-DFM schemes (with $\psi \in \{2/3, 4/3\}$) agree very well with the reference solution. A steep increase in $|\lambda|$ can be seen on the left and right sides of the plot, which implies large in- and outfluxes concentrated at the fracture tips, resulting from the fact that the fracture is much more permeable than the surrounding bulk medium. Small oscillations in λ in the discrete solutions can be seen right at the fracture tips, and we observed these oscillations to stay local within the first adjacent grid cell, not polluting the solution in the entire domain. However, the oscillations are not reflected in the term $(\mathbf{K}\nabla h_2) \cdot \mathbf{n}|_{\gamma_1}$. Furthermore, it is noteworthy that for the EBOX-MORTAR-DFM scheme, the magnitude of the oscillation seems to be slightly increased for $\psi = 4/3$ in comparison to $\psi = 1/3$. Recall that for $\psi = 0.5$, the EBOX-MORTAR-DFM scheme produces the same results as the EBOX-DFM scheme, which is why these results are not included here. Although also not shown here, for $\psi = 1.0$, we observed spurious oscillations in λ across the entire interface, and we will return to this later in the discussion.

Recall that $\lambda \propto \frac{k}{a} (h_1 - h_2)|_{\gamma_1}$ according to condition (11a). Therefore, with the permeability in the fracture being much higher than in the bulk medium, the difference in the hydraulic heads h_2 and h_1 is very small and not visible in the plots shown in the lower row of fig. 14. In particular, due to the above-mentioned proportionality, we expect small oscillations in the hydraulic head to be present at the fracture tips since they are observed in λ . For the EBOX-MORTAR-DFM scheme

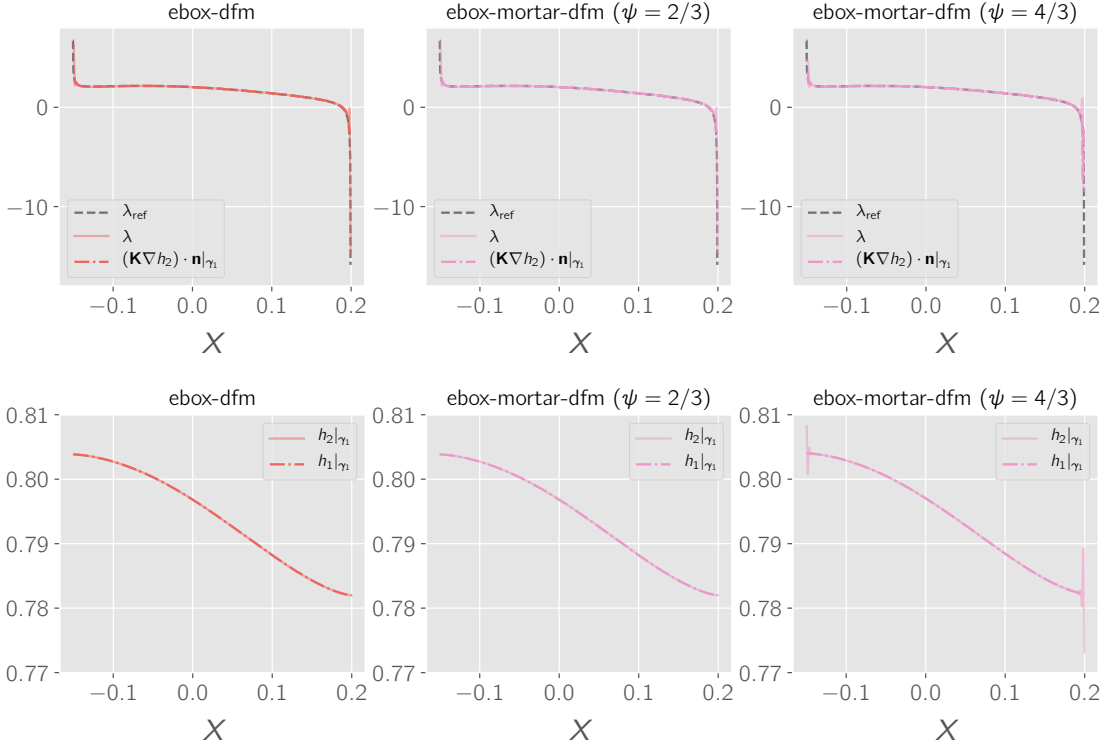


Figure 14: **Case 3.1 - interface flux and hydraulic head.** The top and bottom rows show the transfer fluxes and the hydraulic heads along the interface γ_1 , respectively.

with $\psi > 1$, noticeable oscillations of h_2 appear at the fracture tips, as can be seen in the lower right plot in fig. 14. However, the projections of the hydraulic heads used in eq. (23a), that is, the discrete variant of the condition (11a), seem to level out these oscillations such that they do not strongly influence the transfer flux λ as shown in the plot directly above.

Let us now turn to the case of the continuity conditions (11b) being applied at the bulk-fracture interfaces, for which the results are depicted in fig. 15. As mentioned before, with these conditions the EBOX-MORTAR-DFM scheme leads to singular system matrices for $\psi < 1$. As can be seen in the plots, we consider the case of $\psi = 1$, for which the transfer fluxes λ exhibit spurious oscillations along the entire interface. Since a rather fine grid is used, the oscillations appear as a shaded area in the upper center plot of fig. 15. Note that the y-axis of the plot has been adjusted to match the non-oscillative solution, and the actual magnitude of the oscillations is much larger. It is noteworthy that despite the oscillations in λ , the term $(\mathbf{K}\nabla h_2)|_{\gamma_1}$ is still monotone and fits well to the reference solution. The same holds for the hydraulic heads which are shown in the plot directly below. For a coarser mortar grid, using $\psi = 4/3$, we again observe small oscillations right at the fracture tips of both λ and h_2 , as can be seen in the plots in the right column of fig. 15. The magnitude of the oscillations seems to be smaller when compared to the case of the conditions (11a) (see fig. 14).

As discussed earlier, the EBOX-DFM scheme weakly incorporates the continuity condition (11b), and it can be seen from the lower left plot of fig. 15 that the scheme is able to capture the continuity along the entire interface, except for the fracture tips, where we now observe noticeable differences between $h_2|_{\gamma_1}$ and $h_1|_{\gamma_1}$. Recall that, when the conditions (11b) are used, the bulk-fracture transfer fluxes are assembled independent of the interface head $h_2|_{\gamma_1}$ after eq. (21). Therefore, these deviations do not lead to a deterioration of λ , which is shown in the upper left plot of fig. 15.

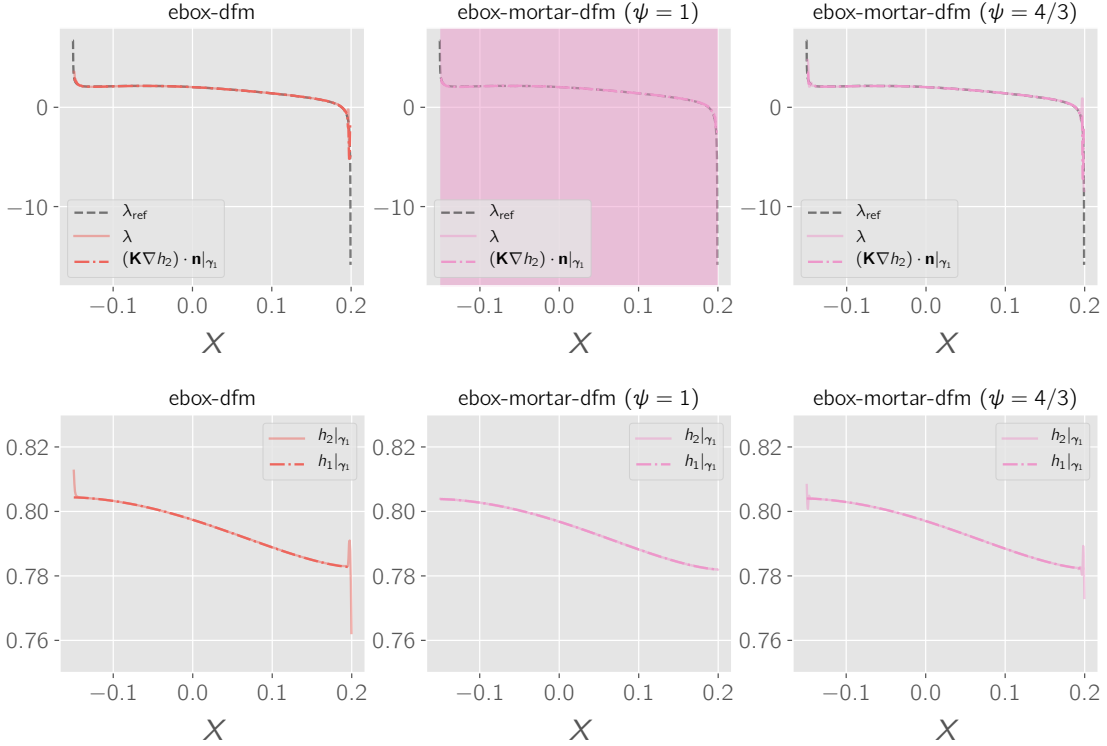


Figure 15: **Case 3.2 - interface flux and hydraulic head.** The top and bottom rows show the transfer fluxes and the hydraulic heads along the interface γ_1 , respectively.

A very good match with the reference solution is again obtained, and it seems that the small oscillations of λ at the fracture tips are even less pronounced than for $\mathcal{S}_{a,c} \equiv \mathcal{S}_{a,b}$ (see fig. 14).

5.4. Two-dimensional benchmark case

This test case is taken from Flemisch et al. (2018) and considers 64 fractures whose orientations were deduced from an image of an outcrop near Bergen, Norway. The domain has a size of $700\text{ m} \times 600\text{ m}$, and a flow from left to right is induced by prescribing $h_2 = h_1 = 1013250\text{ m}$ at $x = 0\text{ m}$, and $h_2 = h_1 = 0\text{ m}$ on the right boundary at $x = 700\text{ m}$. On the top and bottom boundaries, no-flow boundary conditions are prescribed. The permeabilities are set to $\mathbf{K}_2 = 1 \cdot 10^{-14}\text{ I m/s}$ and $\mathbf{K}_1 = k\text{ I m/s}$, where $k = 1 \cdot 10^{-8}$, and an aperture of $a = 1 \cdot 10^{-2}\text{ m}$ is used. In this work, we consider a second variant of the test case with low-permeable fractures using $k = 1 \cdot 10^{-18}$. An illustration of the domain and the numerical solutions for both fracture permeabilities can be found in fig. 16.

As in Flemisch et al. (2018), we want to compare the numerical solutions obtained with the different schemes based on plots over line of the hydraulic head. Figure 17 shows the hydraulic head plotted along the line $x = 625\text{ m}$ for both fracture permeabilities, where we added the numerical solution of the “*Flux-Mortar*” scheme presented in the original study to the plot for $k = 1 \cdot 10^{-8}$ (The data was taken from the associated repository at git.iws.uni-stuttgart.de/benchmarks/fracture-flow/). The scheme uses a mixed-finite element formulation with flux mortars at the bulk-fracture interfaces, more details can be found in Boon et al. (2018).

Figure 17a shows that the solutions obtained with the different schemes in the case of highly-permeable fractures agree very well among each other, except for the one of the BOX-DFM scheme, which leads to slightly higher hydraulic heads in the center part of the plot. This is in agreement with the observations made in Flemisch et al. (2018), where the BOX-DFM scheme, although a

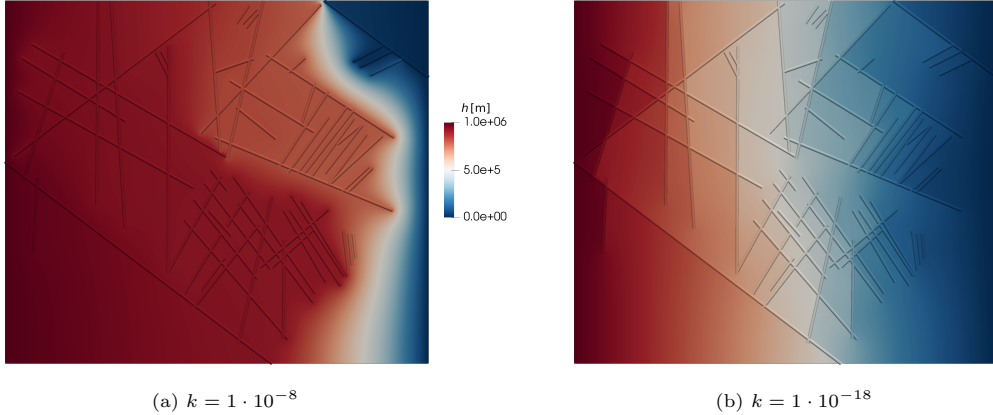


Figure 16: **Case 4 - numerical solutions.** Shown are the solutions obtained with the EBOX-DFM scheme for the case of highly-permeable fractures (a) and low-permeable fractures (b). The fractures are visualized by tubes, colored with the solution for h_1 in the fractures.

different implementation, was also included in the investigations. Moreover, a good match with the results for the “*Flux-Mortar*” scheme of the original study can be seen. Note that in that study, a coarser mesh consisting of 7614 triangles and 867 line elements was used, while in this work we use 113820 triangular and 3618 lines. In the case of low-permeable fractures we see that the BOX-DFM scheme completely fails to capture relevant features of the solution, while the results of the remaining schemes agree rather well (see fig. 17b).

On unstructured simplex grids, a benefit of vertex-centered schemes is that they lead to significantly less degrees of freedom. The numbers for the grid used in this test case are listed in table 3, which shows that approximately two times as many degrees of freedom are used in the cell-centered schemes when compared to the EBOX-DFM scheme. The EBOX-MORTAR-DFM scheme introduces additional degrees of freedom due to discretization of the mortar variable, and the BOX-DFM scheme leads to the smallest number of unknowns. Despite the differences in number of unknowns, the number of nonzero entries in the system matrix for the TPFA-DFM and the EBOX-DFM scheme is very similar due to the small stencils of the TPFA-DFM scheme. However, recall that the TPFA-DFM scheme is inconsistent on unstructured grids and anisotropic permeabilities, while EBOX-DFM has shown to produce results that are comparable to the MPFA-DFM scheme for different permeability angles and contrasts (see section 5.2).

Although leading to results of comparable quality, the MPFA-DFM scheme produces about three times as many nonzero entries in the system matrix as the EBOX-DFM and the EBOX-MORTAR-DFM schemes (see table 3). However, we have tested several iterative linear solvers, and they failed to solve the system arising from the EBOX-MORTAR-DFM scheme, which is why the results shown in fig. 17 were obtained with the direct solver UMFPack (Davis, 2004). Moreover, for large fracture permeabilities, we have experienced iterative linear solver issues also for the EBOX-DFM scheme. This indicates poor conditioning of the system matrix, which might be due to the fact

Table 3: **Case 4 - matrix characteristics.** Number of degrees of freedom (N_{dof}) and number of nonzero entries (N_{nnz}) in the system matrices.

	TPFA-DFM	MPFA-DFM	EBOX-DFM	EBOX-MORTAR-DFM			BOX-DFM
				$\psi = 2/3$	$\psi = 6/5$	$\psi = 2$	
N_{dof}	117 438	117 438	64 403	75 149	70 473	57 160	
$N_{\text{nnz}}(\mathcal{S}_{d,c} \equiv \mathcal{S}_{d,\mathcal{B}})$	473 426	1 537 488	476 245	537 252	500 547	-	-
$N_{\text{nnz}}(\mathcal{S}_{d,c} \equiv \mathcal{S}_{d,\mathcal{H}})$	473 426	1 537 488	455 750	-	494 465	473 491	398 283

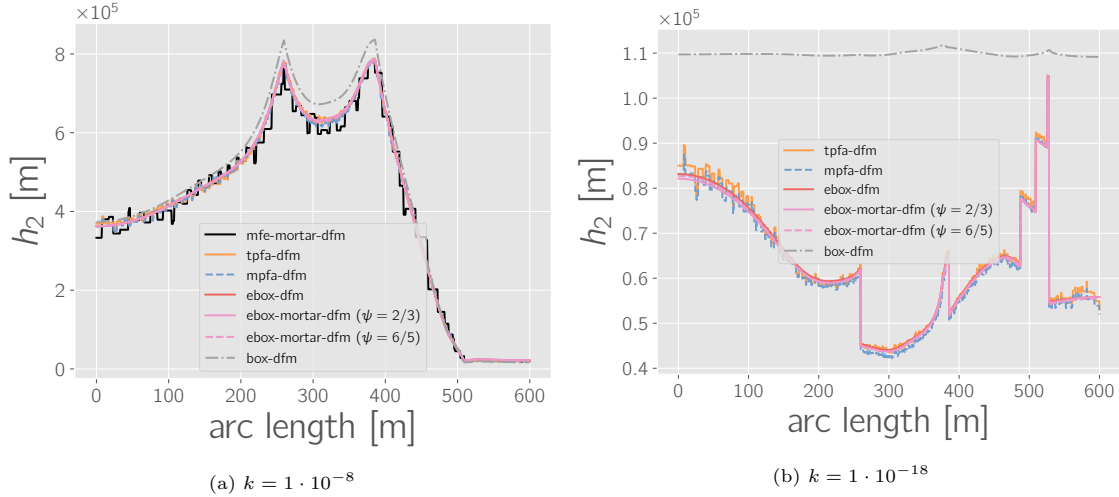


Figure 17: **Case 4 - plots over line.** The figures show the hydraulic head h_2 in the bulk medium, plotted along the line $x = 625$ m. The left plot further depicts the results obtained with the “*Flux-Mortar*” scheme included in the original study (Flemisch et al., 2018), to which it is referred in the legend by “*mfe-mortar-dfm*”.

that in the EBOX-DFM scheme, the bulk-fracture coupling entries scale with k/a as a consequence of condition (11a), while the diagonal block scales with the bulk permeability. This could explain why we observed a deterioration of the iterative linear solver performance with increasing fracture permeability, while this effect was not observed for the cell-centered schemes, where the coupling entries scale with the harmonic mean of the bulk and fracture permeabilities. However, one possible remedy seems to be the use of the conditions (11b) for highly-permeable fractures, for which we have observed better iterative linear solver performance with the EBOX-DFM scheme, while visually indistinguishable results compared to those of fig. 17 were obtained. Please note that a detailed analysis of the performance of iterative linear solvers is not within the scope of this work and should be addressed in future investigations.

5.5. Three-dimensional benchmark case

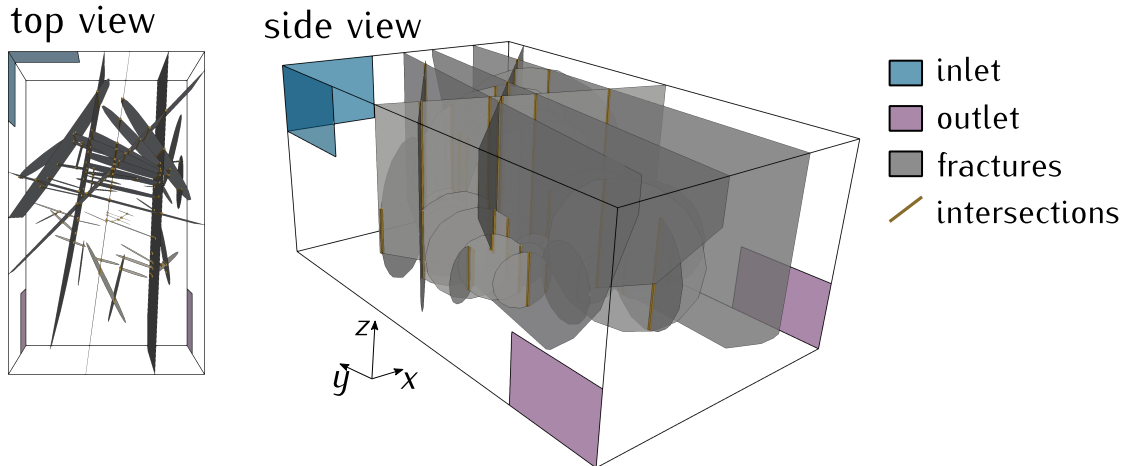


Figure 18: **Case 5 - computational domain.** The figure visualizes the fracture network considered in the three-dimensional benchmark case, which is taken from Berre et al. (2021). Moreover, the inlet and outlet boundary segments are depicted.

This benchmark case is taken from Berre et al. (2021), and it considers a domain with the

dimensions $\Omega = (500 \text{ m}, 350 \text{ m}) \times (100 \text{ m}, 1500 \text{ m}) \times (-100 \text{ m}, 500 \text{ m})$, containing 52 fractures with 106 intersections. The fracture network was again created by postprocessing of an outcrop near Bergen in Norway, and was originally presented in Fumagalli et al. (2019). Figure 18 illustrates the domain and fracture network, and it depicts the inlet and outlet boundaries, where uniform unit inflow and a hydraulic head of $h_2 = 0 \text{ m}$ are set, respectively. The permeabilities are given by $\mathbf{K}_2 = \mathbf{I} \text{ m/s}$ and $\mathbf{K}_1 = 1 \cdot 10^4 \mathbf{I} \text{ m/s}$, and an aperture of $a = 1 \cdot 10^{-2} \text{ m}$ is used.

We use the conditions (11b) at all interfaces, which can be justified by the small aperture and the comparatively large fracture permeability. Comparisons of the solutions for both interface conditions (obtained with the TPFA-DFM scheme) showed that they lead to visually indistinguishable results. By choosing the interface condition (11b), we must choose $\psi > 1$, and here we use $\psi = 4$, which means that each triangle of the discretization of the mortar domain contains exactly four triangles of the fracture grid. An illustration of this is given in fig. 19. Note that the implementation is able to handle nonconforming meshes, however, for this benchmark we have experienced issues with adjusting the geometric tolerance used upon mesh generation with Gmsh (Geuzaine & Remacle, 2009) to that used during mesh intersection in Dumux. Small differences in the geometry due to inaccuracies during mesh generation might appear when generating the meshes used for flow and the mortar domain, respectively. These in turn might result in extremely small intersection segments when the used geometric tolerance does not match. In order avoid such issues, we have generated the mesh used for flow by subdivision of a coarser grid, which has been used for the discretization of the mortar domain. Ongoing work addresses the improvement of the robustness of the intersection algorithms and the choice of optimal geometric tolerances.

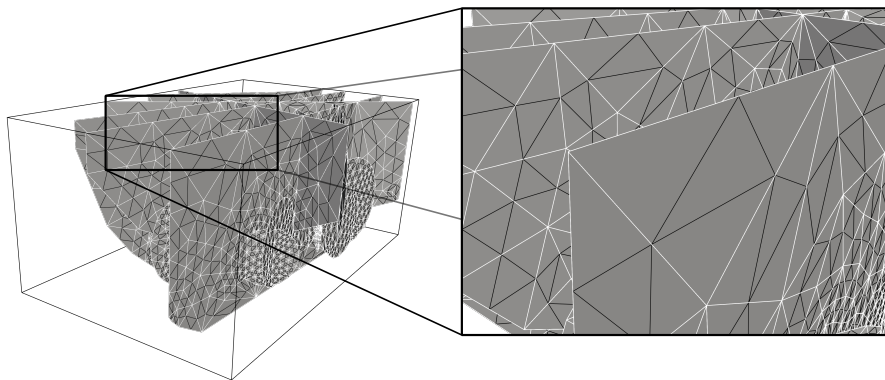


Figure 19: **Case 5 - fracture and mortar grid.** Closeup on the grids used in the fracture and the mortar domains. The black lines show the grid elements of the fracture grids, while the white lines illustrate those of the mortar grid.

We simulate the benchmark with all schemes considered in this work, and we perform simulations both taking into account flow along fracture intersections and assuming continuity after the conditions (10). An exception is the BOX-DFM scheme, for which the current implementation in DuMu^x does not allow for flow along intersections. Figure 20 shows plots of the hydraulic head h_2 along two different lines, both of which are used as metrics of comparison in the original study Berre et al. (2021). The depicted results correspond to the simulations neglecting intersection flow, however, visually indistinguishable plots were obtained when taking it into account, which is why we do not present them here. In this benchmark, the fracture intersections are all oriented vertically, and thus, orthogonal to the direction of flow. For other orientations or for larger permeability contrasts, taking into account flow along intersections might have a significant impact on the overall flow field (see, for example, Gläser (2020)). The plots further show the results of the “*UiB-MVEM*” scheme, which uses a formulation on the basis of mixed virtual elements and is one of the schemes considered in the original study Berre et al. (2021). For further details on the scheme we refer to Fumagalli & Keilegavlen (2019). The results were taken from the data

repository associated with the publication (git.iws.uni-stuttgart.de/benchmarks/fracture-flow-3d), and they were originally produced with an implementation provided in the open-source numerical simulation tool PorePy (Keilegavlen et al., 2020).

In the first plot (fig. 20a), we can see that a good match of the hydraulic head was obtained among the different schemes, and that they fit well to the reference curve of the original study. However, significantly larger hydraulic heads are obtained with the TPFA-DFM scheme. Note that the TPFA-DFM scheme, using the implementation provided in PorePy, was also taken into account in Berre et al. (2021), where the respective curve was much closer to those of the other schemes. But, here we are using a different grid, which is constructed by refinement of an initial discretization in order to obtain the desired refinement ratio of $\psi = 4$ between the grids used for flow and the mortar grid. The properties of the resulting mesh might again promote the inconsistency of the scheme, as was the case also in section 5.2.

A rather good match is obtained with the BOX-DFM scheme, which leads to only slightly lower hydraulic heads. However, the deviations are a bit more pronounced in the second plot shown in fig. 20b, where we again observe that the schemes presented in this work lead to very similar results, although slightly larger deviations to the reference curve are visible. But as mentioned, we do not use the same grid as in the original study and the deviations might decrease upon further grid refinement.

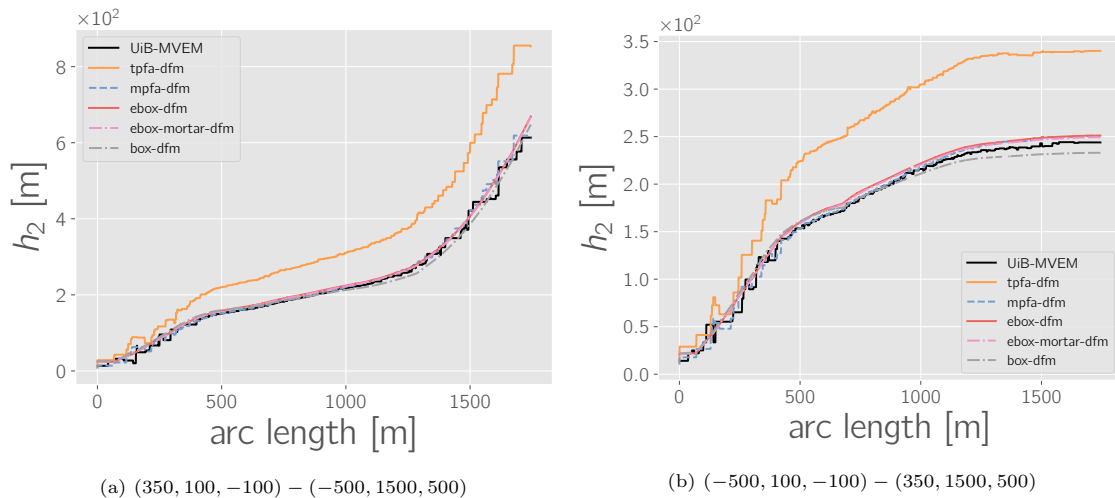


Figure 20: **Case 5 - plots over line.** The figures show the hydraulic head h_2 in the bulk medium, plotted along two different lines as given in the captions. The results shown here correspond to those simulations in which flow along fracture intersections was neglected. Moreover, the plots include the results obtained with the “*UiB-MVEM*” scheme presented in the benchmark study Berre et al. (2021).

A comparison of the computational cost of the different schemes is given in table 4. It is noteworthy that on the three-dimensional unstructured grid used here, the ratio of degrees of freedom for cell-centered and vertex-centered schemes is significantly higher than in the two-dimensional case (see section 5.4). Besides that, the MPFA-DFM scheme leads to substantially more nonzero entries in the linear system matrix, when compared to the other schemes, as a result of its large stencils on unstructured simplex grids. In particular, the system matrix of the MPFA-DFM scheme contains about 15 times more nonzero entries than those of the EBOX-DFM and EBOX-MORTAR-DFM schemes, which has strong implications on the computational efficiency of the schemes. Despite these differences, they produce very similar results (see fig. 20).

Table 4: **Case 5 - matrix characteristics.** Number of degrees of freedom (N_{dof}) and number of nonzero entries (N_{nnz}) in the system matrices of the different schemes. Results are shown for the case of considering ($\Omega_1 \neq \emptyset$) and neglecting ($\Omega_1 = \emptyset$) flow along intersections.

	TPFA-DFM	MPFA-DFM	EBOX-DFM	EBOX-MORTAR-DFM	BOX-DFM
$\Omega_1 = \emptyset$					
N_{dof}	320 004	320 004	86 409	105 835	47 700
N_{nnz}	1 640 238	21 639 021	1 390 232	1 492 260	707 930
$\Omega_1 \neq \emptyset$					
N_{dof}	321 028	321 028	90 315	111 603	
N_{nnz}	1 640 490	21 677 870	1 433 077	1 527 509	

6. Summary and outlook

In this work we have presented a comparison, by means of numerical experiments, of different finite volume schemes for the simulation of flow in fractured porous media. The underlying mathematical model is based on a mixed-dimensional formulation in which the bulk medium, the fractures and intersections of fractures are described by geometries of decreasing dimensionality. On each of these subdomains, an individual system of partial differential equations is solved and the interaction between them is described by fluxes across interior boundaries and via source terms on the lower-dimensional features.

Several well-established schemes were considered, namely the cell-centered TPFA-DFM and MPFA-DFM schemes (Karimi-Fard et al., 2004; Sandve et al., 2012; Ahmed et al., 2015) and the vertex-centered BOX-DFM scheme (Reichenberger et al., 2006). However, the mathematical formulation of the latter differs from the one presented in this work in several aspects, as it assumes continuity of the hydraulic head across the fractures and does not explicitly describe the bulk-fracture mass exchange. Therefore, we have introduced an extension of the latter in this work, the EBOX-DFM scheme, which is able to capture the discontinuities in the hydraulic head and the fluxes that potentially occur across the fractures. In this scheme, the bulk-fracture transfer fluxes are expressed in terms of the hydraulic heads in the two subdomains and the coupling conditions are incorporated weakly. We have furthermore introduced the EBOX-MORTAR-DFM scheme, in which the transfer fluxes appear as additional unknowns, allowing for a strong incorporation of the desired coupling conditions at subdomain interfaces.

We have studied the performance of the different schemes on various two- and three-dimensional test cases. The convergence behaviour against analytical and equi-dimensional reference solutions was investigated, and we have applied the schemes to two- and three-dimensional benchmark cases taken from the literature. Optimal convergence was observed for the newly-introduced schemes and we have found a good agreement of the numerical results to those presented in the original benchmark studies. Moreover, we observed that the solutions obtained with EBOX-DFM and EBOX-MORTAR-DFM schemes were comparable to those of the MPFA-DFM scheme while being computationally much more efficient. In general, cell-centered schemes lead to many more degrees of freedom than vertex-centered schemes on unstructured simplex grids. Furthermore, the MPFA-DFM scheme involves very large stencils, especially on three-dimensional grids, which leads to a large number of non-zero entries in the system matrices. In this regard, the presented vertex-centered schemes show to be a promising alternative, producing consistent results with less computational effort.

However, we have observed that several iterative linear solvers struggled to solve the systems arising from the EBOX-DFM and EBOX-MORTAR-DFM schemes, especially for large fracture permeabilities. Therefore, we have used a direct solver in this work. Future investigations could be targetted at developing iterative linear solvers that are well-suited for solving the systems arising

from these schemes. Moreover, the performance of the schemes in the context of two-phase flow could be studied in future work, which is of high relevance in a variety of geotechnical applications. In multiphase settings, we expect that the importance of the numerical schemes being able to capture discontinuities across the fractures is even more pronounced, as jumps in saturations and capillary pressures occur at material interfaces. While the cell-centered schemes and the BOX-DFM scheme have already been applied to two-phase flow (see e.g. Reichenberger et al. (2006); Gläser et al. (2017)), it might be more difficult to derive a formulation for the EBOX-MORTAR-DFM scheme. Two-phase flow models typically involve non-linearities, and therefore, it would be of particular interest to study the convergence behaviour of non-linear solvers for the different numerical schemes.

Acknowledgements

We thank the Deutsche Forschungsgemeinschaft (DFG, German Research Foundation) for supporting this work by funding SFB 1313, Project Number 327154368.

References

- Aavatsmark, I. (2002). An introduction to multipoint flux approximations for quadrilateral grids. *Computational Geosciences*, 6, 405–432. doi:10.1023/A:1021291114475.
- Ahmed, R., Edwards, M., Lamine, S., Huisman, B., & Pal, M. (2015). Control-volume distributed multi-point flux approximation coupled with a lower-dimensional fracture model. *Journal of Computational Physics*, 284, 462 – 489. doi:10.1016/j.jcp.2014.12.047.
- Ahmed, R., Edwards, M. G., Lamine, S., Huisman, B. A., & Pal, M. (2017). Cvd-mpfa full pressure support, coupled unstructured discrete fracture–matrix darcy-flux approximations. *Journal of Computational Physics*, 349, 265 – 299. doi:10.1016/j.jcp.2017.07.041.
- Antonietti, P. F., Formaggia, L., Scotti, A., Verani, M., & Verzott, N. (2016). Mimetic finite difference approximation of flows in fractured porous media. *ESAIM: Mathematical Modelling and Numerical Analysis*, 50, 809–832. doi:10.1051/m2an/2015087.
- Berkowitz, B. (2002). Characterizing flow and transport in fractured geological media: A review. *Advances in Water Resources*, 25, 861–884. doi:10.1016/S0309-1708(02)00042-8.
- Berre, I., Boon, W. M., Flemisch, B., Fumagalli, A., Gläser, D., Keilegavlen, E., Scotti, A., Stefansson, I., Tatomir, A., Brenner, K., Burbulla, S., Devloo, P., Duran, O., Favino, M., Hennicker, J., Lee, I.-H., Lipnikov, K., Masson, R., Mosthaf, K., Nestola, M. G. C., Ni, C.-F., Nikitin, K., Schädle, P., Svyatskiy, D., Yanbarisov, R., & Zulian, P. (2021). Verification benchmarks for single-phase flow in three-dimensional fractured porous media. *Advances in Water Resources*, 147, 103759. doi:10.1016/j.advwatres.2020.103759.
- Boon, W. M., Nordbotten, J. M., & Yotov, I. (2018). Robust discretization of flow in fractured porous media. *SIAM Journal on Numerical Analysis*, 56, 2203–2233. doi:10.1137/17M1139102.
- Brenner, K., Hennicker, J., Roland, M., & Samier, P. (2016). Gradient discretization of hybrid-dimensional darcy flow in fractured porous media with discontinuous pressures at matrix–fracture interfaces. *IMA Journal of Numerical Analysis*, 37. doi:10.1093/imanum/drw044.
- Davis, T. A. (2004). Algorithm 832: Umfpack v4.3—an unsymmetric-pattern multifrontal method. *ACM Trans. Math. Softw.*, 30, 196–199. doi:10.1145/992200.992206.
- Flemisch, B., Berre, I., Boon, W., Fumagalli, A., Schwenck, N., Scotti, A., Stefansson, I., & Tatomir, A. (2018). Benchmarks for single-phase flow in fractured porous media. *Advances in Water Resources*, 111, 239 – 258. doi:10.1016/j.advwatres.2017.10.036.

- Flemisch, B., Darcis, M., Erbertseder, K., Faigle, B., Lauser, A., Mosthaf, K., Müthing, S., Nuske, P., Tatomir, A., Wolff, M., & Helmig, R. (2011). Dumux: Dune for multi-Phase, Component, Scale, Physics, ... flow and transport in porous media. *Advances in Water Resources*, *34*, 1102–1112. doi:10.1016/j.advwatres.2011.03.007.
- Flemisch, B., Fumagalli, A., & Scotti, A. (2016). A review of the xfem-based approximation of flow in fractured porous media. *Advances in Discretization Methods*, *12*, 47–76. doi:10.1007/978-3-319-41246-7_3.
- Fumagalli, A., & Keilegavlen, E. (2019). Dual virtual element methods for discrete fracture matrix models. *Oil & Gas Science and Technology - Revue d'IFP Energies nouvelles*, *74*, 41. doi:10.2516/ogst/2019008.
- Fumagalli, A., Keilegavlen, E., & Scialò, S. (2019). Conforming, non-conforming and non-matching discretization couplings in discrete fracture network simulations. *Journal of Computational Physics*, *376*, 694 – 712. doi:10.1016/j.jcp.2018.09.048.
- Geuzaine, C., & Remacle, J.-F. (2009). Gmsh: A 3-d finite element mesh generator with built-in pre- and post-processing facilities. *International Journal for Numerical Methods in Engineering*, *79*, 1309–1331. doi:10.1002/nme.2579.
- Gläser, D. (2020). *Discrete fracture modeling of multi-phase flow and deformation in fractured poroelastic media*. phdthesis Universität Stuttgart. URL: <https://elib.uni-stuttgart.de/handle/11682/11057>. doi:10.18419/opus-11040.
- Gläser, D., Flemisch, B., Helmig, R., & Class, H. (2019). A hybrid-dimensional discrete fracture model for non-isothermal two-phase flow in fractured porous media. *GEM-International Journal on Geomathematics*, *10*, 5. doi:10.1007/s13137-019-0116-8.
- Gläser, D., Helmig, R., Flemisch, B., & Class, H. (2017). A discrete fracture model for two-phase flow in fractured porous media. *Advances in Water Resources*, *110*, 335 – 348. doi:doi.org/10.1016/j.advwatres.2017.10.031.
- Hackbusch, W. (1989). On first and second order box schemes. *Computing*, *41*, 277–296. doi:10.1007/BF02241218.
- Hægland, H., Assteerawatt, A., Dahle, H. K., Eigestad, G. T., & Helmig, R. (2009). Comparison of cell-and vertex-centered discretization methods for flow in a two-dimensional discrete-fracture-matrix system. *Advances in Water resources*, *32*, 1740–1755. doi:10.1016/j.advwatres.2009.09.006.
- Helmig, R. (1997). *Multiphase flow and transport processes in the subsurface: a contribution to the modeling of hydrosystems..* Springer-Verlag.
- Jaeger, J., Cook, N., & Zimmerman, R. (2007). *Fundamentals of Rock Mechanics*. Wiley.
- Karimi-Fard, M., Durlofsky, L., & Aziz, K. (2004). An efficient discrete-fracture model applicable for general-purpose reservoir simulators. *SPE Journal*, *9*, 227–236. doi:10.2118/79699-MS.
- Kazemi, H., Merrill Jr, L., Porterfield, K., Zeman, P. et al. (1976). Numerical simulation of water-oil flow in naturally fractured reservoirs. *Society of Petroleum Engineers Journal*, *16*, 317–326. doi:10.2118/5719-PA.
- Keilegavlen, E., Berge, R., Fumagalli, A., Starnoni, M., Stefansson, I., Varela, J., & Berre, I. (2020). Porepy: an open-source software for simulation of multiphysics processes in fractured porous media. *Computational Geosciences*, (pp. 1–23). doi:10.1007/s10596-020-10002-5.

- Koch, T., Gläser, D., Weishaupt, K., Ackermann, S., Beck, M., Becker, B., Burbulla, S., Class, H., Coltman, E., Emmert, S., Fetzner, T., Grüninger, C., Heck, K., Hommel, J., Kurz, T., Lipp, M., Mohammadi, F., Scherrer, S., Schneider, M., Seitz, G., Stadler, L., Utz, M., Weinhardt, F., & Flemisch, B. (2020). DuMu^x 3 - an open-source simulator for solving flow and transport problems in porous media with a focus on model coupling. *Computers & Mathematics with Applications*, . doi:10.1016/j.camwa.2020.02.012.
- Köppel, M., Martin, V., Jaffré, J., & Roberts, J. E. (2018). A lagrange multiplier method for a discrete fracture model for flow in porous media. *Computational Geosciences*, (pp. 1–15). doi:10.1007/s10596-018-9779-8.
- Lisjak, A., Tatone, B., Mahabadi, O., Grasselli, G., Marschall, P., Lanyon, G., de La Vaissière, R., Shao, H., Leung, H., & Nussbaum, C. (2016). Hybrid finite-discrete element simulation of the edz formation and mechanical sealing process around a microtunnel in opalinus clay. *Rock Mechanics and Rock Engineering*, 49. doi:10.1007/s00603-015-0847-2.
- Martin, V., Jaffré, J., & Roberts, J. E. (2005). Modeling fractures and barriers as interfaces for flow in porous media. *SIAM Journal on Scientific Computing*, 26, 1667–1691. doi:10.1137/S1064827503429363.
- Matthai, S. K., Mezentsev, A., & Belayneh, M. (2007). Finite element - node-centered finite-volume two-phase-flow experiments with fractured rock represented by unstructured hybrid-element meshes. *Society of Petroleum Engineers*, . doi:10.2118/93341-PA.
- Nordbotten, J. M., Boon, W. M., Fumagalli, A., & Keilegavlen, E. (2019). Unified approach to discretization of flow in fractured porous media. *Computational Geosciences*, 23, 225–237. doi:10.1007/s10596-018-9778-9.
- Pruess, K. (1992). *Brief Guide to the MINC-method for Modeling Flow and Transport in Fractured Media*. United States. Department of Energy. doi:10.2172/6951290.
- Pruess, K., Wang, J., & Tsang, Y. (1990). On thermohydrologic conditions near high-level nuclear wastes emplaced in partially saturated fractured tuff: 2. effective continuum approximation. *Water Resources Research*, 26, 1249–1261. doi:10.1029/WR026i006p01249.
- Reichenberger, V., Jakobs, H., Bastian, P., & Helmig, R. (2006). A mixed-dimensional finite volume method for two-phase flow in fractured porous media. *Advances in Water Resources*, 29, 1020–1036. doi:10.1016/j.advwatres.2005.09.001.
- Royer, P., Auriault, J.-L., Lewandowska, J., & Serres, C. (2002). Continuum modelling of contaminant transport in fractured porous media. *Transport in Porous Media*, 49, 333–359. doi:10.1023/A:1016272700063.
- Sandve, T., Berre, I., & Nordbotten, J. (2012). An efficient multi-point flux approximation method for discrete fracture–matrix simulations. *Journal of Computational Physics*, 231, 3784 – 3800. doi:10.1016/j.jcp.2012.01.023.
- Schwenck, N., Flemisch, B., Helmig, R., & Wohlmuth, B. (2015). Dimensionally reduced flow models in fractured porous media: crossings and boundaries. *Computational Geosciences*, 19. doi:10.1007/s10596-015-9536-1.
- Schädle, P., Zulian, P., Vogler, D., Bhopalam, S. R., Nestola, M. G., Ebigbo, A., Krause, R., & Saar, M. O. (2019). 3d non-conforming mesh model for flow in fractured porous media using lagrange multipliers. *Computers & Geosciences*, 132, 42 – 55. doi:10.1016/j.cageo.2019.06.014.
- Tatomir, A.-B. (2012). *From discrete to continuum concepts of flow in fractured porous media*. Ph.D. thesis Universitätsbibliothek der Universität Stuttgart Holzgartenstr. 16, 70174 Stuttgart. doi:10.18419/opus-476.

- Tene, M., Bosma, S. B., Kobaisi, M. S. A., & Hajibeygi, H. (2017). Projection-based embedded discrete fracture model (pedfm). *Advances in Water Resources*, *105*, 205 – 216. doi:10.1016/j.advwatres.2017.05.009.
- Ucar, E., Berre, I., & Keilegavlen, E. (2018). Three-dimensional numerical modeling of shear stimulation of fractured reservoirs. *Journal of Geophysical Research: Solid Earth*, *123*, 3891–3908. doi:10.1029/2017JB015241.
- Walton, K. M., Unger, A. J. A., Ioannidis, M. A., & Parker, B. L. (2017). Impact of eliminating fracture intersection nodes in multiphase compositional flow simulation. *Water Resources Research*, *53*, 2917–2939. doi:10.1002/2016WR020088.
- Warren, J., & Root, P. (1963). The behavior of naturally fractured reservoirs. *Society of Petroleum Engineers Journal*, *3*, 245–255.
- Wohlmuth, B. (2011). Variationally consistent discretization schemes and numerical algorithms for contact problems. *Acta Numerica*, *20*, 569–734. doi:10.1017/S0962492911000079.
- Zimmerman, R. W., Chen, G., Hadgu, T., & Bodvarsson, G. S. (1993). A numerical dual-porosity model with semianalytical treatment of fracture/matrix flow. *Water resources research*, *29*, 2127–2137. doi:10.1029/93WR00749.

Appendix

Table 5: **Case 2 - errors and rates of h_2 for $\Theta = 0$.** Listed are the errors ε_{h_2} and the corresponding rates r_{h_2} over grid refinement, expressed in terms of η_f .

η_f	TPFA-DFM		MPFA-DFM		EBOX-DFM		EBOX-MORTAR-DFM		BOX-DFM		
	ε_{h_2}	r_{h_2}	ε_{h_2}	r_{h_2}	ε_{h_2}	r_{h_2}	ε_{h_2}	r_{h_2}	ε_{h_2}	r_{h_2}	
$k = 1 \cdot 10^4$											
\mathcal{F}_1	2.43e-02	2.12e-01		1.40e-01		1.55e-01		1.52e-01		1.55e-01	
	1.21e-02	1.64e-01	3.67e-01	6.78e-02	1.04e+00	7.25e-02	1.10e+00	7.05e-02	1.11e+00	7.26e-02	1.10e+00
	6.07e-03	1.44e-01	1.94e-01	3.22e-02	1.07e+00	3.51e-02	1.04e+00	3.40e-02	1.05e+00	3.53e-02	1.04e+00
	3.04e-03	1.32e-01	1.19e-01	1.47e-02	1.13e+00	1.65e-02	1.09e+00	1.58e-02	1.10e+00	1.67e-02	1.08e+00
	1.52e-03	1.36e-01	-3.73e-02	6.26e-03	1.23e+00	7.34e-03	1.17e+00	6.91e-03	1.20e+00	7.56e-03	1.15e+00
	7.59e-04	1.33e-01	3.35e-02	2.95e-03	1.08e+00	3.49e-03	1.07e+00	3.26e-03	1.08e+00	3.73e-03	1.02e+00
\mathcal{F}_2	2.25e-02	2.42e-01		1.53e-01		2.01e-01		1.86e-01		2.01e-01	
	1.12e-02	1.72e-01	4.95e-01	7.82e-02	9.71e-01	9.71e-02	1.05e+00	9.10e-02	1.03e+00	9.75e-02	1.04e+00
	5.62e-03	5.40e-01	-1.65e+00	3.93e-02	9.93e-01	4.87e-02	9.95e-01	4.56e-02	9.98e-01	4.92e-02	9.88e-01
	2.81e-03	1.33e-01	2.03e+00	1.93e-02	1.02e+00	2.41e-02	1.02e+00	2.24e-02	1.03e+00	2.45e-02	1.01e+00
	1.41e-03	4.94e-01	-1.90e+00	9.17e-03	1.07e+00	1.15e-02	1.07e+00	1.06e-02	1.08e+00	1.19e-02	1.04e+00
	7.03e-04	2.45e-01	1.01e+00	4.35e-03	1.08e+00	5.37e-03	1.10e+00	4.89e-03	1.12e+00	5.81e-03	1.04e+00
\mathcal{F}_3	1.70e-02	2.16e-01		1.33e-01		1.79e-01		1.65e-01		1.75e-01	
	8.52e-03	1.76e-01	3.01e-01	6.69e-02	9.86e-01	8.63e-02	1.05e+00	7.88e-02	1.07e+00	8.46e-02	1.05e+00
	4.26e-03	1.50e-01	2.29e-01	3.28e-02	1.03e+00	4.63e-02	8.98e-01	4.20e-02	9.10e-01	4.67e-02	8.57e-01
	2.13e-03	2.40e-01	-6.79e-01	1.62e-02	1.02e+00	2.60e-02	8.33e-01	2.36e-02	8.33e-01	2.81e-02	7.31e-01
	1.06e-03	1.09e+00	-2.19e+00	8.93e-03	8.60e-01	1.54e-02	7.58e-01	1.41e-02	7.39e-01	1.90e-02	5.65e-01
	5.32e-04	1.52e-01	2.84e+00	6.69e-03	4.17e-01	1.01e-02	6.03e-01	9.56e-03	5.62e-01	1.49e-02	3.57e-01
$k = 1 \cdot 10^{-4}$											
\mathcal{F}_1	2.43e-02	2.35e-01		1.58e-01		1.45e-01		1.45e-01		1.96e-01	
	1.21e-02	1.84e-01	3.50e-01	8.29e-02	9.28e-01	6.66e-02	1.12e+00	6.66e-02	1.12e+00	1.50e-01	3.81e-01
	6.07e-03	1.60e-01	2.02e-01	4.20e-02	9.79e-01	3.14e-02	1.08e+00	3.14e-02	1.08e+00	1.40e-01	1.09e-01
	3.04e-03	1.44e-01	1.52e-01	2.09e-02	1.01e+00	1.43e-02	1.14e+00	1.43e-02	1.14e+00	1.37e-01	2.59e-02
	1.52e-03	1.35e-01	9.82e-02	1.08e-02	9.61e-01	6.11e-03	1.22e+00	6.11e-03	1.22e+00	1.37e-01	5.00e-03
	7.59e-04	1.28e-01	7.88e-02	6.48e-03	7.31e-01	3.47e-03	8.17e-01	3.47e-03	8.17e-01	1.37e-01	4.65e-04
\mathcal{F}_2	2.25e-02	2.68e-01		2.06e-01		1.49e-01		1.49e-01		2.13e-01	
	1.12e-02	2.41e-01	1.55e-01	1.05e-01	9.73e-01	7.20e-02	1.05e+00	7.19e-02	1.05e+00	1.71e-01	3.22e-01
	5.62e-03	2.10e-01	1.96e-01	5.15e-02	1.03e+00	3.51e-02	1.04e+00	3.51e-02	1.04e+00	1.59e-01	1.02e-01
	2.81e-03	2.12e-01	-1.15e-02	2.55e-02	1.01e+00	1.67e-02	1.07e+00	1.67e-02	1.07e+00	1.56e-01	2.79e-02
	1.41e-03	8.99e-01	-2.09e+00	1.31e-02	9.65e-01	7.62e-03	1.13e+00	7.62e-03	1.13e+00	1.55e-01	7.37e-03
	7.03e-04	2.04e-01	2.14e+00	7.39e-03	8.23e-01	3.86e-03	9.81e-01	3.86e-03	9.81e-01	1.55e-01	1.97e-03
\mathcal{F}_3	1.70e-02	1.52e-01		1.29e-01		1.19e-01		1.19e-01		2.43e-01	
	8.52e-03	1.54e-01	-2.27e-02	6.22e-02	1.05e+00	4.99e-02	1.25e+00	4.99e-02	1.25e+00	2.13e-01	1.87e-01
	4.26e-03	1.13e-01	4.48e-01	2.90e-02	1.10e+00	2.35e-02	1.09e+00	2.35e-02	1.09e+00	2.07e-01	4.40e-02
	2.13e-03	1.12e-01	7.10e-03	1.48e-02	9.75e-01	1.21e-02	9.57e-01	1.21e-02	9.56e-01	2.05e-01	1.13e-02
	1.06e-03	1.24e-01	-1.36e-01	9.47e-03	6.41e-01	8.17e-03	5.65e-01	8.17e-03	5.66e-01	2.05e-01	3.12e-03
	5.32e-04	5.01e-01	-2.02e+00	8.04e-03	2.36e-01	7.48e-03	1.28e-01	7.47e-03	1.28e-01	2.05e-01	9.23e-04

Table 6: **Case 2 - errors and rates of h_1** for $\Theta = 0$. Listed are the errors ε_{h_1} and the corresponding rates r_{h_1} over grid refinement, expressed in terms of η_f .

η_f	TPFA-DFM		MPFA-DFM		EBOX-DFM		EBOX-MORTAR-DFM		BOX-DFM		
	ε_{h_1}	r_{h_1}	ε_{h_1}	r_{h_1}	ε_{h_1}	r_{h_1}	ε_{h_1}	r_{h_1}	ε_{h_1}	r_{h_1}	
$k = 1 \cdot 10^4$											
\mathcal{F}_1	2.43e-02	1.15e-01		3.75e-02		6.51e-02		6.30e-02		6.02e-02	
	1.21e-02	8.54e-02	4.32e-01	1.47e-02	1.35e+00	2.09e-02	1.64e+00	2.00e-02	1.65e+00	1.80e-02	1.74e+00
	6.07e-03	7.12e-02	2.64e-01	5.22e-03	1.49e+00	7.01e-03	1.58e+00	6.64e-03	1.59e+00	5.77e-03	1.64e+00
	3.04e-03	6.53e-02	1.24e-01	3.30e-03	6.63e-01	3.45e-03	1.02e+00	3.36e-03	9.81e-01	4.19e-03	4.62e-01
	1.52e-03	5.39e-02	2.77e-01	3.10e-03	8.78e-02	2.92e-03	2.42e-01	2.92e-03	2.03e-01	4.24e-03	-1.81e-02
	7.59e-04	5.39e-02	-2.01e-04	3.05e-03	2.36e-02	2.91e-03	2.51e-03	2.92e-03	-1.68e-03	4.25e-03	-1.55e-03
\mathcal{F}_2	2.25e-02	1.14e-01		3.25e-02		6.52e-02		6.77e-02		5.22e-02	
	1.12e-02	6.41e-02	8.25e-01	7.58e-03	2.10e+00	2.47e-02	1.40e+00	2.70e-02	1.33e+00	1.54e-02	1.76e+00
	5.62e-03	9.66e-01	-3.91e+00	4.15e-03	8.70e-01	9.36e-03	1.40e+00	1.06e-02	1.34e+00	4.81e-02	1.68e+00
	2.81e-03	5.66e-02	4.09e+00	4.14e-03	3.25e-03	4.57e-03	1.03e+00	5.17e-03	1.04e+00	4.96e-03	-4.21e-02
	1.41e-03	1.02e-02	2.48e+00	3.80e-03	1.23e-01	3.46e-03	4.03e-01	3.67e-03	4.96e-01	5.24e-03	-7.93e-02
	7.03e-04	2.21e-01	-4.44e+00	3.57e-03	8.85e-02	3.31e-03	6.21e-02	3.38e-03	1.19e-01	5.15e-03	2.43e-02
\mathcal{F}_3	1.70e-02	7.42e-02		2.20e-02		1.18e-01		1.16e-01		8.49e-02	
	8.52e-03	6.27e-02	2.45e-01	1.94e-02	1.79e-01	5.99e-02	9.81e-01	5.66e-02	1.03e+00	3.08e-02	1.46e+00
	4.26e-03	5.29e-02	2.44e-01	1.85e-02	7.03e-02	3.21e-02	9.00e-01	3.02e-02	9.06e-01	2.29e-02	4.25e-01
	2.13e-03	8.13e-02	-6.20e-01	1.67e-02	1.45e-01	1.79e-02	8.42e-01	1.70e-02	8.30e-01	2.39e-02	-6.19e-02
	1.06e-03	1.19e-01	-5.54e-01	1.51e-02	1.50e-01	1.22e-02	5.61e-01	1.21e-02	4.87e-01	2.46e-02	-3.91e-02
	5.32e-04	5.90e-02	1.02e+00	1.41e-02	9.17e-02	1.20e-02	1.46e-02	1.22e-02	-5.12e-03	2.48e-02	-1.16e-02
$k = 1 \cdot 10^{-4}$											
\mathcal{F}_1	2.43e-02	1.93e-01		5.04e-02		5.97e-02		5.96e-02		5.48e-02	
	1.21e-02	1.54e-01	3.28e-01	2.15e-02	1.23e+00	2.02e-02	1.56e+00	2.01e-02	1.57e+00	1.88e-02	1.54e+00
	6.07e-03	1.33e-01	2.09e-01	8.55e-03	1.33e+00	7.58e-03	1.41e+00	7.56e-03	1.41e+00	1.58e-02	2.54e-01
	3.04e-03	1.19e-01	1.53e-01	3.69e-03	1.21e+00	3.62e-03	1.07e+00	3.61e-03	1.07e+00	1.78e-02	-1.73e-01
	1.52e-03	1.07e-01	1.53e-01	1.97e-03	9.06e-01	2.33e-03	6.35e-01	2.33e-03	6.32e-01	1.89e-02	-9.08e-02
	7.59e-04	1.01e-01	8.78e-02	1.74e-03	1.77e-01	2.04e-03	1.87e-01	2.05e-03	1.87e-01	1.95e-02	-4.28e-02
\mathcal{F}_2	2.25e-02	2.40e-01		1.84e-01		9.49e-02		8.44e-02		2.43e-01	
	1.12e-02	2.04e-01	2.32e-01	9.34e-02	9.80e-01	5.02e-02	9.17e-01	4.40e-02	9.41e-01	2.34e-01	5.34e-02
	5.62e-03	1.97e-01	4.93e-02	4.87e-02	9.39e-01	2.82e-02	8.32e-01	2.60e-02	7.60e-01	2.31e-01	2.02e-02
	2.81e-03	2.03e-01	-4.01e-02	2.92e-02	7.35e-01	1.81e-02	6.42e-01	1.77e-02	5.52e-01	2.30e-01	7.35e-03
	1.41e-03	2.58e-01	-3.47e-01	1.80e-02	7.01e-01	1.12e-02	6.87e-01	1.11e-02	6.80e-01	2.29e-01	3.00e-03
	7.03e-04	1.88e-01	4.59e-01	1.06e-02	7.56e-01	6.97e-03	6.89e-01	6.81e-03	7.00e-01	2.29e-01	1.33e-03
\mathcal{F}_3	1.70e-02	1.31e-01		9.83e-02		8.89e-02		8.25e-02		2.25e-01	
	8.52e-03	9.04e-02	5.31e-01	5.33e-02	8.84e-01	4.22e-02	1.08e+00	3.97e-02	1.06e+00	2.12e-01	8.45e-02
	4.26e-03	1.24e-01	-4.59e-01	3.43e-02	6.35e-01	2.91e-02	5.34e-01	2.91e-02	4.48e-01	2.09e-01	2.32e-02
	2.13e-03	1.28e-01	-4.56e-02	2.65e-02	3.71e-01	2.33e-02	3.24e-01	2.36e-02	3.03e-01	2.08e-01	7.11e-03
	1.06e-03	1.48e-01	-2.05e-01	2.05e-02	3.71e-01	1.86e-02	3.25e-01	1.86e-02	3.45e-01	2.07e-01	2.73e-03
	5.32e-04	5.12e-01	-1.79e+00	1.71e-02	2.65e-01	1.65e-02	1.68e-01	1.65e-02	1.70e-01	2.07e-01	1.20e-03

Table 7: **Case 2 - errors and rates of h_2** for $\Theta = \pi/4$. Listed are the errors ε_{h_2} and the corresponding rates r_{h_2} over grid refinement, expressed in terms of η_f .

η_f	TPFA-DFM		MPFA-DFM		EBOX-DFM		EBOX-MORTAR-DFM		BOX-DFM		
	ε_{h_2}	r_{h_2}	ε_{h_2}	r_{h_2}	ε_{h_2}	r_{h_2}	ε_{h_2}	r_{h_2}	ε_{h_2}	r_{h_2}	
$k = 1 \cdot 10^4$											
\mathcal{F}_1	2.43e-02	1.82e-01		1.53e-01		1.65e-01		1.62e-01		1.65e-01	
	1.21e-02	1.01e-01	8.53e-01	7.25e-02	1.08e+00	7.86e-02	1.07e+00	7.63e-02	1.08e+00	7.89e-02	1.07e+00
	6.07e-03	6.88e-02	5.53e-01	3.47e-02	1.06e+00	3.84e-02	1.04e+00	3.69e-02	1.05e+00	3.86e-02	1.03e+00
	3.04e-03	5.83e-02	2.37e-01	1.61e-02	1.11e+00	1.82e-02	1.08e+00	1.73e-02	1.09e+00	1.84e-02	1.07e+00
	1.52e-03	5.60e-02	5.90e-02	6.92e-03	1.22e+00	8.05e-03	1.18e+00	7.51e-03	1.20e+00	8.22e-03	1.16e+00
	7.59e-04	8.88e-02	-6.64e-01	3.30e-03	1.07e+00	3.70e-03	1.12e+00	3.42e-03	1.14e+00	3.86e-03	1.09e+00
\mathcal{F}_2	2.25e-02	1.86e-01		1.65e-01		1.99e-01		1.89e-01		2.00e-01	
	1.12e-02	1.18e-01	6.59e-01	8.30e-02	9.92e-01	9.79e-02	1.03e+00	9.38e-02	1.01e+00	9.85e-02	1.02e+00
	5.62e-03	8.88e-02	4.10e-01	4.17e-02	9.93e-01	4.81e-02	1.02e+00	4.61e-02	1.02e+00	4.86e-02	1.02e+00
	2.81e-03	9.28e-02	-6.37e-02	2.02e-02	1.04e+00	2.32e-02	1.05e+00	2.22e-02	1.06e+00	2.35e-02	1.04e+00
	1.41e-03	8.63e-02	1.05e-01	9.37e-03	1.11e+00	1.08e-02	1.11e+00	1.02e-02	1.11e+00	1.11e-02	1.08e+00
	7.03e-04	7.36e-02	2.31e-01	4.33e-03	1.11e+00	4.95e-03	1.12e+00	4.68e-03	1.13e+00	5.33e-03	1.06e+00
\mathcal{F}_3	1.70e-02	2.53e-01		1.33e-01		1.78e-01		1.63e-01		1.81e-01	
	8.52e-03	2.11e-01	2.64e-01	6.92e-02	9.46e-01	8.66e-02	1.04e+00	8.00e-02	1.02e+00	8.88e-02	1.03e+00
	4.26e-03	4.47e-01	-1.08e+00	3.38e-02	1.03e+00	4.30e-02	1.01e+00	3.97e-02	1.01e+00	4.54e-02	9.69e-01
	2.13e-03	1.89e-01	1.24e+00	1.61e-02	1.07e+00	2.17e-02	9.89e-01	2.00e-02	9.92e-01	2.46e-02	8.85e-01
	1.06e-03	2.03e-01	-1.05e-01	8.27e-03	9.64e-01	1.17e-02	8.93e-01	1.08e-02	8.82e-01	1.53e-02	6.84e-01
	5.32e-04	2.81e-01	-4.70e-01	5.86e-03	4.98e-01	7.65e-03	6.09e-01	7.31e-03	5.68e-01	1.18e-02	3.78e-01
$k = 1 \cdot 10^{-4}$											
\mathcal{F}_1	2.43e-02	1.68e-01		1.43e-01		1.49e-01		1.49e-01		1.49e-01	
	1.21e-02	9.64e-02	8.05e-01	6.77e-02	1.08e+00	6.83e-02	1.12e+00	6.83e-02	1.12e+00	6.94e-02	1.10e+00
	6.07e-03	6.87e-02	4.89e-01	3.22e-02	1.07e+00	3.21e-02	1.09e+00	3.21e-02	1.09e+00	3.41e-02	1.02e+00
	3.04e-03	5.94e-02	2.09e-01	1.47e-02	1.13e+00	1.45e-02	1.14e+00	1.45e-02	1.14e+00	1.84e-02	8.92e-01
	1.52e-03	5.68e-02	6.55e-02	6.09e-03	1.27e+00	5.99e-03	1.28e+00	5.99e-03	1.28e+00	1.27e-02	5.36e-01
	7.59e-04	6.65e-02	-2.28e-01	2.77e-03	1.14e+00	2.68e-03	1.16e+00	2.68e-03	1.16e+00	1.15e-02	1.44e-01
\mathcal{F}_2	2.25e-02	1.62e-01		1.46e-01		1.49e-01		1.49e-01		2.15e-01	
	1.12e-02	1.16e-01	4.85e-01	7.81e-02	9.03e-01	7.04e-02	1.08e+00	7.04e-02	1.08e+00	1.72e-01	3.21e-01
	5.62e-03	1.04e-01	1.63e-01	4.11e-02	9.25e-01	3.40e-02	1.05e+00	3.40e-02	1.05e+00	1.62e-01	9.46e-02
	2.81e-03	1.19e-01	-1.97e-01	2.13e-02	9.47e-01	1.59e-02	1.09e+00	1.59e-02	1.09e+00	1.59e-01	2.46e-02
	1.41e-03	1.00e-01	2.49e-01	1.16e-02	8.80e-01	7.44e-03	1.10e+00	7.44e-03	1.10e+00	1.58e-01	6.31e-03
	7.03e-04	1.05e-01	-7.10e-02	7.36e-03	6.55e-01	4.54e-03	7.12e-01	4.54e-03	7.12e-01	1.58e-01	1.68e-03
\mathcal{F}_3	1.70e-02	1.36e-01		1.30e-01		1.13e-01		1.13e-01		2.12e-01	
	8.52e-03	1.05e-01	3.77e-01	5.86e-02	1.15e+00	4.88e-02	1.21e+00	4.88e-02	1.21e+00	1.78e-01	2.56e-01
	4.26e-03	1.64e-01	-6.41e-01	2.81e-02	1.06e+00	2.34e-02	1.06e+00	2.35e-02	1.06e+00	1.70e-01	6.22e-02
	2.13e-03	9.47e-02	7.91e-01	1.37e-02	1.04e+00	1.20e-02	9.61e-01	1.20e-02	9.61e-01	1.68e-01	1.51e-02
	1.06e-03	1.11e-01	-2.26e-01	7.51e-03	8.65e-01	7.51e-03	6.82e-01	7.51e-03	6.82e-01	1.68e-01	3.74e-03
	5.32e-04	4.34e-01	-1.97e+00	5.81e-03	3.72e-01	6.27e-03	2.59e-01	6.27e-03	2.60e-01	1.68e-01	9.02e-04

Table 8: **Case 2 - errors and rates of h_1** for $\Theta = \pi/4$. Listed are the errors ε_{h_1} and the corresponding rates r_{h_1} over grid refinement, expressed in terms of η_f .

η_f	TPFA-DFM		MPFA-DFM		EBOX-DFM		EBOX-MORTAR-DFM		BOX-DFM		
	ε_{h_1}	r_{h_1}	ε_{h_1}	r_{h_1}	ε_{h_1}	r_{h_1}	ε_{h_1}	r_{h_1}	ε_{h_1}	r_{h_1}	
$k = 1 \cdot 10^4$											
\mathcal{F}_1	2.43e-02	2.83e-02		3.76e-02		8.00e-02		7.93e-02		7.58e-02	
	1.21e-02	4.15e-02	-5.52e-01	6.69e-03	2.49e+00	1.40e-02	2.51e+00	1.43e-02	2.47e+00	1.44e-02	2.39e+00
	6.07e-03	4.62e-02	-1.53e-01	3.15e-03	1.08e+00	2.22e-03	2.66e+00	2.52e-03	2.51e+00	4.26e-03	1.76e+00
	3.04e-03	4.91e-02	-8.77e-02	2.88e-03	1.30e-01	2.12e-03	7.16e-02	2.22e-03	1.84e-01	3.76e-03	1.80e-01
	1.52e-03	5.07e-02	-4.78e-02	2.79e-03	4.49e-02	2.40e-03	-1.81e-01	2.45e-03	-1.41e-01	3.78e-03	-7.47e-03
	7.59e-04	5.92e-02	-2.23e-01	2.74e-03	2.66e-02	2.54e-03	-8.17e-02	2.56e-03	-6.71e-02	3.77e-03	2.32e-03
\mathcal{F}_2	2.25e-02	1.47e-02		1.41e-02		1.14e-02		2.95e-02		3.06e-03	
	1.12e-02	3.27e-02	-1.15e+00	5.70e-03	1.31e+00	1.53e-03	2.89e+00	7.88e-03	1.90e+00	4.70e-03	-6.18e-01
	5.62e-03	3.37e-02	-4.14e-02	3.34e-03	7.71e-01	2.61e-03	-7.69e-01	2.75e-03	1.52e+00	4.30e-03	1.27e-01
	2.81e-03	3.00e-02	1.67e-01	3.15e-03	8.52e-02	2.87e-03	-1.36e-01	2.49e-03	1.44e-01	4.03e-03	9.20e-02
	1.41e-03	7.12e-02	-1.25e+00	3.03e-03	5.65e-02	2.82e-03	2.36e-02	2.67e-03	-1.00e-01	4.02e-03	6.06e-03
	7.03e-04	3.99e-02	8.37e-01	2.94e-03	4.31e-02	2.81e-03	6.18e-03	2.76e-03	-4.93e-02	4.00e-03	7.81e-03
\mathcal{F}_3	1.70e-02	2.34e-01		2.10e-02		2.56e-02		3.56e-02		2.02e-02	
	8.52e-03	2.12e-01	1.46e-01	1.50e-02	4.81e-01	1.43e-02	8.43e-01	1.66e-02	1.10e+00	1.83e-02	1.46e-01
	4.26e-03	3.69e-01	-8.00e-01	1.29e-02	2.26e-01	1.01e-02	4.95e-01	1.12e-02	5.74e-01	1.94e-02	-8.68e-02
	2.13e-03	1.71e-01	1.11e+00	1.19e-02	1.11e-01	9.50e-03	9.08e-02	1.00e-02	1.55e-01	1.99e-02	-3.51e-02
	1.06e-03	2.10e-01	-2.97e-01	1.14e-02	6.55e-02	9.93e-03	-6.35e-02	1.02e-02	-1.87e-02	2.00e-02	-7.08e-03
	5.32e-04	1.72e-01	2.85e-01	1.11e-02	3.34e-02	1.04e-02	-6.20e-02	1.05e-02	-4.40e-02	1.99e-02	5.60e-03
$k = 1 \cdot 10^{-4}$											
\mathcal{F}_1	2.43e-02	1.04e-01		4.25e-02		7.92e-02		7.92e-02		8.08e-02	
	1.21e-02	9.59e-02	1.23e-01	9.07e-03	2.23e+00	1.65e-02	2.27e+00	1.65e-02	2.27e+00	1.90e-02	2.09e+00
	6.07e-03	9.51e-02	1.26e-02	3.13e-03	1.54e+00	4.06e-03	2.02e+00	4.06e-03	2.02e+00	6.33e-03	1.58e+00
	3.04e-03	9.17e-02	5.17e-02	1.55e-03	1.01e+00	1.75e-03	1.22e+00	1.75e-03	1.21e+00	3.38e-03	9.06e-01
	1.52e-03	8.83e-02	5.47e-02	1.01e-03	6.27e-01	1.05e-03	7.30e-01	1.05e-03	7.30e-01	2.20e-03	6.19e-01
	7.59e-04	7.09e-02	3.17e-01	8.15e-04	3.03e-01	8.22e-04	3.58e-01	8.22e-04	3.59e-01	1.63e-03	4.29e-01
\mathcal{F}_2	2.25e-02	1.23e-01		8.41e-02		9.30e-02		8.50e-02		2.52e-01	
	1.12e-02	1.37e-01	-1.52e-01	5.37e-02	6.47e-01	4.11e-02	1.18e+00	3.65e-02	1.22e+00	2.32e-01	1.18e-01
	5.62e-03	1.50e-01	-1.33e-01	3.78e-02	5.06e-01	2.52e-02	7.09e-01	2.41e-02	5.96e-01	2.26e-01	3.57e-02
	2.81e-03	1.50e-01	4.43e-03	2.80e-02	4.34e-01	1.83e-02	4.58e-01	1.85e-02	3.81e-01	2.25e-01	1.13e-02
	1.41e-03	1.49e-01	9.06e-03	2.00e-02	4.85e-01	1.34e-02	4.47e-01	1.35e-02	4.54e-01	2.24e-01	4.03e-03
	7.03e-04	1.55e-01	-6.24e-02	1.41e-02	5.05e-01	1.04e-02	3.66e-01	1.04e-02	3.78e-01	2.24e-01	1.60e-03
\mathcal{F}_3	1.70e-02	1.05e-01		1.05e-01		7.09e-02		6.55e-02		2.09e-01	
	8.52e-03	1.03e-01	4.08e-02	4.49e-02	1.22e+00	3.50e-02	1.02e+00	3.30e-02	9.88e-01	1.98e-01	8.03e-02
	4.26e-03	1.29e-01	-3.27e-01	3.00e-02	5.81e-01	2.50e-02	4.88e-01	2.51e-02	3.94e-01	1.96e-01	1.55e-02
	2.13e-03	1.04e-01	3.00e-01	2.35e-02	3.53e-01	2.01e-02	3.10e-01	2.06e-02	2.88e-01	1.95e-01	4.43e-03
	1.06e-03	1.20e-01	-2.01e-01	1.81e-02	3.74e-01	1.63e-02	3.06e-01	1.64e-02	3.28e-01	1.95e-01	1.72e-03
	5.32e-04	1.73e-01	-5.27e-01	1.51e-02	2.61e-01	1.47e-02	1.44e-01	1.48e-02	1.52e-01	1.95e-01	7.49e-04